steel research international
www.steel-research.de

In Situ Investigation of Microstructure Evolution and Stress Generation During Low-Pressure Carburizing and Quenching by Means of Synchrotron X-Ray Diffraction

*Ogün Baris Tapar, Michael Georg Zürn, Jens Gibmeier, Antonio Carlos de Figueiredo Silveira, Matthias Steinbacher, Norbert Schell, and Jérémy Epp**

Low-pressure carburizing (LPC) is a thermochemical process that enriches steel surfaces with carbon. While LPC is already used in industry, there are still aspects that offer opportunities for optimization if the necessary basic process understanding is provided. The present study quantifies the effect of LPC process parameters on the material state of different steel grades. For this purpose, in situ carburizing and quenching experiments are performed in a custom-built chamber for synchrotron X-ray diffraction at the German Electron Synchrotron in Hamburg. During carbon enrichment, carbon saturation and carbide formation are observed, slowing acetylene decomposition. Carbides that initially form at the surface dissolve in later diffusion steps. The kinetics of carbide formation and dissolution strongly depend on steel grade and carbide size. Quenching experiments further enable systematic analysis of phase-specific stresses at the surface and subsurface. The influence of transformation temperature across the carbon gradient is tracked, revealing differences in maximum stresses in both austenite and martensite. A direct correlation is identified between the local martensite fraction and the generated stresses within the carburized layer. This work provides new experimental insights into carbon uptake, carbide evolution, and stress development during LPC, offering pathways for process optimization across different steel types.

1. Introduction

Low-pressure carburizing (LPC), or vacuum carburizing, is a thermochemical process that modifies the chemical composition of the near-surface region of the material by carbon enrichment.[1] The purpose of the process is to achieve a hard, wear-resistant surface while maintaining high core ductility.[2]

During LPC, components are initially heated to a predefined carburizing temperature using a nitrogen atmosphere up to 800 °C and then heated further under vacuum. Subsequently, a carbon-donor gas is introduced into the furnace at controlled pressures ranging from 1 to 30 mbar. In this stage, carbon atoms dissociate, adsorb onto the surface, and diffuse into the material, resulting in an increased carbon concentration at the surface layer of the workpiece.[1] This carbon enrichment stage is referred to as the "boost" step. Following this, the furnace is evacuated of residual gases, and carbon diffusion from the surface into the core commences, leading to the formation of a carbon gradient (CG). This stage is known as the "diffusion" step. The boost and diffusion steps can be repeated cyclically until the desired carbon profile is achieved. Process parameters, including temperature, the number and duration of boost/diffusion steps, the gas flow rate, and the pressure, can be varied to obtain the foreseen case depth and carbon distribution. Upon achieving the targeted carbon profile, components are typically quenched using high-pressurized inert gases, such as helium or nitrogen.

O. B. Tapar, A. C. F. Silveira, M. Steinbacher, J. Epp
Division Materials Engineering
Leibinz Institute for Materials Engineering - IWT
Badgasteiner Str. 3, 28359 Bremen, Germany
E-mail: epp@iwt-bremen.de

The ORCID identification number(s) for the author(s) of this article can be found under https://doi.org/10.1002/srin.202501083.

DOI: 10.1002/srin.202501083

M. G. Zürn, J. Gibmeier
Karlsruhe Institute of Technology
Institute for Applied Materials (IAM-WK)
Engelbert-Arnold-Str. 4, 76131 Karlsruhe, Germany

N. Schell
Institute of Materials Physics
Helmholtz-Zentrum Hereon
Max-Planck-Straße 1, 21502 Geesthacht, Germany

M. Steinbacher, J. Epp
MAPEX Centre for Materials and Processes
University of Bremen
Badgasteiner Str. 3, 28359 Bremen, Germany

Several hydrocarbon gases can be used as carbon-donor gases, such as propane, methane, or acetylene. However, LPC using acetylene is particularly advantageous in terms of economic and environmental considerations due to its reduced soot formation.[3,4] Moreover, it is more efficient, since pyrolysis of acetylene predominantly yields carbon and hydrogen rather than other hydrocarbon gases.[5,6]

Despite its advantages, the LPC process presents particular challenges. Due to its nonequilibrium nature, the relationship between the process parameters and the behavior of the workpiece under treatment is not completely understood. As a result, process parameters are often determined in advance through trial-and-error experiments, which rely on previously established carbon profiles. These experiments typically require a substantial number of input variables to develop generalized predictions. Although the LPC process has been in commercial use for over 50 years,[7] and extensive data have become available, the underlying mechanisms continue to be the subject of study, that is, a profound comprehension of the process is still lacking.

Gorockiewicz explained the kinetics of carbon absorption and diffusion by analyzing two steels containing high- and low-alloy content,[8] and also analyzed the structure of the carbon layer formed on the surface of the sample.[9] Kwon et al. investigated the effect of alloying elements on carbon diffusion behavior, revealing that the presence of chromium influences carbon diffusion by promoting carbide formation at the surface.[10] Wołowiec-Korecka et al. focused on the effect of the gas flow rate and the process pressure on the carburized layer and reported that the carbon content in the carburized specimens increases with the gas flow rate in the low-pressure range (1–3 mbar). However, they observed the opposite trend at higher pressures (5–7 mbar).[11]

In addition to parameter analyses, several attempts were made to introduce a generalized model to describe LPC. Tanaka et al. coupled the finite difference method in conjunction with the CALPHAD software to model carbon and cementite profiles.[12] Yada et al. proposed a numerical model that takes into account both gas and solid phases.[5] The models gave results of carbon content evolution comparable to those obtained with electron microprobe analyses (EMPA). Zajusz et al.[13] developed a model based on the bivelocity method which comprises both the diffusion and drift velocity, the latter being equivalent to lattice velocity. The model proposes a formula to calculate the concentration-dependent diffusion coefficient of carbon and offers comparable predictions of the final CG for low-alloy steels.

Although current studies explain the kinetics of the process and proposed models showed comparable results, the works in literature essentially focus on low- and medium-alloy steels, making the results of complex process variations deviate from the predictions for high-alloy steels. To address this gap, recent studies have increasingly focused on LPC of high-alloy steels. For example, An et al.[14] showed that carbide formation at the surface is significantly affected by the grain size for 18CrNiMo7-6 steel. Similarly, Wang et al.[15] proposed process variations to eliminate a carbide network at the material surface for the 16Cr3NiWMoVNb gear steel. The suggested process variation involves multiple short carburizing pulses along with increasing diffusion time. The authors argue that shorter pulsing steps prevent austenite from reaching the solubility limit and eliminate carbide formation. Moreover, Yin et al.[16] investigated the LPC behavior of the 14Cr14Co13Mo4 steel, while He et al.[17] focused on the ultrahigh alloy 15Cr14Co12Mo5Ni2W steel. Both studies highlighted that the types of formed carbides vary at different depths from the surface, affecting further carburization. They also stated that the predominant observed carbide structures are $M_{23}C_6$ and M_7C_3, where M is the carbide-forming metal.

The given studies provide valuable insights into the phenomenon for specific high-alloy steels and propose models. However, the applicability of these models is often restricted to the specific steels under investigation and typically requires extensive trial-and-error processes when attempting to extend the models to other steel types. Additionally, methods are often limited to post-process examinations, restricting the collection of comprehensive data that represent the entire process. Furthermore, interruption of the process for sample analysis through cooling to predict the material state at high temperature introduces irreversible changes in material properties, making it unrepresentative of its actual state at high temperature.

To overcome these difficulties, detailed knowledge about local carbon enrichment, carbide formation/dissolution kinetics and carbon diffusion must be gained for different alloy compositions.

Achieving this level of understanding is only possible by real-time monitoring of the LPC process, combined with spatially resolved analysis.

High-energy synchrotron X-ray diffraction (HEXRD) is a powerful technique for revealing microstructure evolution and transformation kinetics. Over the last decade, it has been widely used for various heat treatment processes. For instance, Esin et al.[18] described the global progress of austenitization and individual evolutions of phases for slow ($0.25\,^{\circ}C\,s^{-1}$) and fast ($100\,^{\circ}C\,s^{-1}$) heating. Villa et al.[19] investigated the martensitic transformation at subzero temperatures. The authors observed large compressive stresses developed in the remaining austenite, which contributed to the stabilization of austenite. Pickering et al.[20] performed synchrotron measurements to investigate the continuous cooling transformation behaviors of two different steels subjected to austenitization and following quenching. Furthermore, similar to the present study in terms of quantification of volume fractions and carbon-dependent relative changes of lattice parameters, experiments focusing on phase transformations and carbon partitioning are also well documented in the literature.[21–24] Additionally, with regard to in situ analyses of carburized steels at high temperatures, only a limited number of studies focusing on precarburized samples are available in the literature.[25,26] Despite intense studies in recent years, in situ investigation of LPC, including subsequent quenching, to the best of the authors' knowledge, has not yet been conducted.

Previous work by the authors of the article showed the reliability and reproducibility of the developed system, demonstrated the feasibility of synchrotron-based investigations during LPC and provided fundamental data on phase transformations and carbon evolution during the LPC process.[27] However, the investigations were limited to only the common steel grade (20MnCr5) and subjected to several experimental issues such as X-ray beam shifts from the probed position due to temperature variations. This, for example, affected the accurate determination of the evolution of carbides at the surface, which is a crucial aspect of the process.

Building upon those findings, the present work employs an enhanced experimental setup that brings higher measurement accuracy. Therefore, the aim with these new investigations is to deepen the understanding of LPC kinetics, which helps improve the precision of predictive models and ultimately enhance process efficiency. Furthermore, this study also aims to provide real-time experimental data of carbon content evolution, the phase fractions and the phase-specific stress evolution in different steel grades. These findings can serve as a valuable foundation for future research, particularly for simulation-based studies that seek to model the LPC.

2. Experimental Section

2.1. Sample Preparation

Investigations were performed for four different steel grades. The chemical compositions of the steels measured by spark optical emission spectroscopy (S-OES) are given in **Table 1**.

The selected grades represent industrially relevant case-hardening steels with increasing alloying elements that cover a wide compositional spectrum making them suitable for examining the influence of alloy content on LPC kinetics and stress generation during quenching.

The samples were machined into rectangular prism shapes with dimensions of 5 mm thickness, 14 mm length, and 14 mm width. In order to eliminate carbon diffusion from nontarget sides during the in situ experiments, five surfaces of the samples were PVD coated with 5–8 µm thick zirconium nitride (ZrN), leaving only the top surface uncoated for defined carburization.

The effectiveness of the coating was verified by comparing the carbon diffusion depth profiles of both coated and uncoated samples after the carburization process in an industrial furnace. Details of the results were presented in previous work.[27]

2.2. Experimental Setup

The LPC process chamber, specially designed for in situ synchrotron X-ray diffraction studies, is produced from tubular 304 stainless steel. Two circular windows were precision-machined along the beam path for transmission measurement. Additionally, a third window was integrated at the top of the chamber to allow for laser triangulation measurements, enabling precise adjustments of the sample position to account for thermal expansion and contraction of the sample and the sample holder. The beam windows were sealed with ISO-KF flanges covered with 75 µm thick Kapton tape, while the laser triangulation window was covered with 2 mm thick borosilicate glass. The total volume of the chamber, including all pipes, was around 2 L.

Acetylene (C_2H_2) was utilized as a carbon-donor gas, and helium (He) served as a purging and quenching gas. The gas inlet pipe was positioned at the top, while the vacuum outlet pipe was placed at the bottom to ensure that the samples remained within the central portion of the gas flow. The gas supplies of the process were regulated with two mass flow controllers managed by a Protherm 510 process control unit from United Process Controls GmbH/Germany. Pressure levels were monitored via a capacitance manometer and adjusted using a remotely operated electropneumatic valve. In order to avoid any damage caused by high helium pressure during quenching in the case of failure of a vacuum pump or electropneumatic valve, a safety valve set to an opening pressure of 33 mbar was connected to the chamber, which ensured the maximum pressure of 33 mbar during the boost step. A schematic drawing of the sample and a picture of the experimental setup are presented in **Figure 1**.

The sample was heated up in a vacuum using four SiN ceramic heating elements surrounding the sample (see Figure 1a) and connected to an external power supply. The temperature was monitored using a K-type mantle thermocouple inserted into a hole at the side of the sample. Regulation of the temperature through power supply and the recording of the data were done using a Eurotherm temperature controller. All electrical components inside the chamber were constructed from copper-free material to eliminate any risk of acetylide formation, since acetylides are sensitive to temperature and friction and bear a risk of explosion.[28]

Throughout the entire process, the relative position of the carburized surface was measured by using the model ILD1900-50 laser triangulation device from Micro-Epsilon Messtechnik Gmbh, Ortenburg, Germany. The process chamber was mounted on a hexapod of type M-840 from Physik Instrumente (PI)/Germany. The position data measured by the laser triangulation device were simultaneously transmitted to the hexapod which corrected the position of the chamber accordingly, in order to maintain a constant sample surface position relative to the synchrotron beam, that is, to compensate for thermal expansion affecting the sample position. To eliminate continuous and abrupt movements of the chamber caused by the hexapod, the measurement data were smoothed over the last 10 s, and the hexapod moved only at surface displacements above 5 µm. This strategy increased the precision of the measurements of the target position during the entire process. The M-840 hexapod mounted on the heavy load hexapod was only used to adjust the change of surface sample position due to thermal expansion/contraction of the system, while the comparably slower heavy load hexapod was utilized to change measurement positions or to scan the sample along the depth (see the red dashed arrow in Figure 1a).

Table 1. Chemical composition of steels used in mass% (ma%).

Steel grade	Abbr.	C	Si	Mn	Cr	Mo	Ni	V	Al	Cu
20MnCr5	20Mn	0.21	0.28	1.35	1.091	0.03	0.13	0.01	0.03	0.05
14NiCrMo13-4	14Ni	0.1	0.24	0.54	1.22	0.1	3.18	<0.01	0.04	0.08
18CrNiMo7-6	18Cr	0.2	0.18	0.53	1.64	0.3	1.49	0.01	0.03	0.12
Pyrowear 53	Pw53	0.12	0.87	0.31	0.92	3.50	1.85	0.01	0.01	2.24

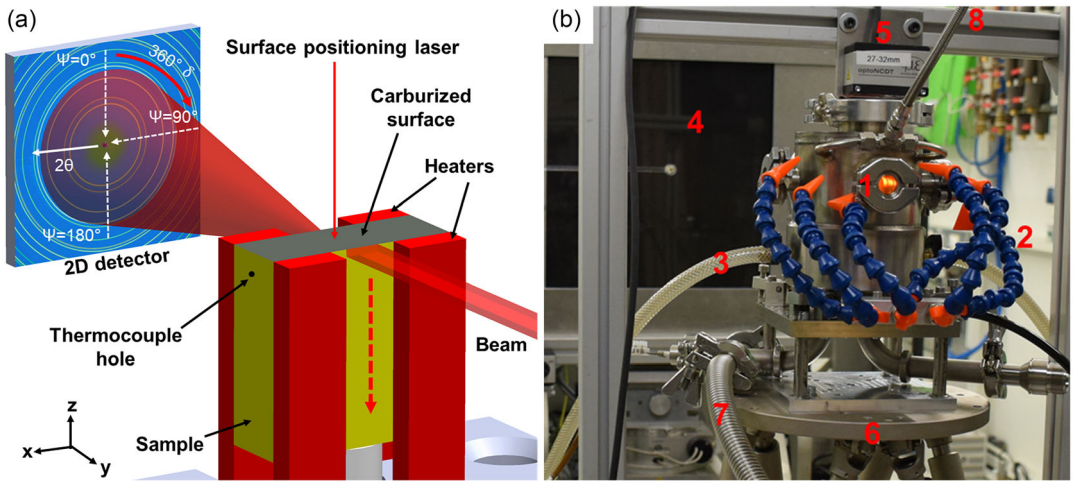

Figure 1. a) Drawing of the sample in transmission mode. Red dashed arrows represent vertical scan direction. b) Experimental apparatus during the LPC process. The numbers on the picture show 1) beam in window, 2) air cooling for the top, 3) water cooling for bottom, 4) 2D detector, 5) laser triangulation device, 6) M-840 hexapod, 7) gas outlet and vacuum pipe, and 8) gas inlet pipe.

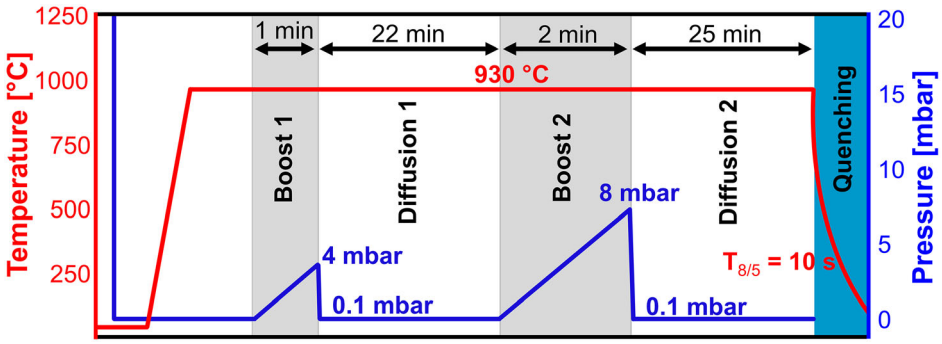

Figure 2. Process scheme of the LPC process with subsequent quenching.

2.3. In Situ Synchrotron Experiments

The LPC process scheme during in situ measurements is given in **Figure 2**. At the beginning of each process, the chamber was evacuated until the pressure of 10^{-1} mbar was reached.

The sample was then heated up to process temperature with an average heating rate of around 160 °C min^{-1} and held for 2 min for homogenization at 930 °C. Upon completion of the holding period, the first boost step was initiated by introducing acetylene into the chamber with a 10 mL min^{-1} flow rate. Due to the small volume of the chamber, pressure could not be regulated during the boost step and therefore continuously increased around 4 mbar per minute. Following the end of the first boost step, the chamber was evacuated of the remaining gases, and the sample was maintained at process temperature for the diffusion step, expanding the carburized region into the depth of the sample. This sequence constituted one complete boost and diffusion cycle. The boost and diffusion cycles were repeated according to the defined process parameters to reach the desired carbon profile. After completion of the required cycles, the sample was quenched below 60 °C using helium gas with 6 bar pressure.

The above-mentioned process parameters, such as the process temperature and duration of the boost/diffusion step, varied depending on the experimental plan given in **Table 2**. The measurements were categorized into three groups named "acetylene

Table 2. LPC process variations.

Designation	Process	Measured steel grades	Process temperature [°C]
Acetylene amount variations			
LA	1/22..2/25..Q	20Mn Pw53	930
HA	2/22..4/25..Q	20Mn Pw53	930
Carbon gradient variations			
CG-1	2/6..Q	18Cr	930
CG-2	2/12..Q	18Cr	930
CG-3	2/24..Q	18Cr	930
Direct quench variations			
DQ	5/0..Q	20Mn Pw53, 18Cr, 14Ni	930

amount variations," "carbon gradient variations," and "direct quench (DQ) variations."

The designations LA, HA, CG, and DQ correspond to low acetylene, high acetylene, carbon gradient, and direct quench, respectively. Numbers associated with these process variations indicate the duration of the boost/diffusion cycles. For example, the process variation LA involves 1 min. of boost followed by 22 min of diffusion as a first cycle, as illustrated in Figure 2. Each boost-diffusion cycle is separated with double dots (..), and the letter "Q" represents the quenching to finalize the process. All samples were heated to the process temperature over an 8 min period and maintained at this temperature for an additional 2 min before the first cycle. Additionally, quenching time for all samples was set to 2 min with high-pressure He. Sample abbreviations and variation designations will be referenced throughout the article for clarity (see Table 1). For example, "LA-20Mn" means it is that the LA variation of the 20MnCr5 steel grade sample.

The in situ synchrotron experiments were carried out at the Deutsches Elektronen-Synchrotron (DESY) at Beamline P07-EH3 of the PETRA III storage ring with a 103.3 keV monochromatic X-ray beam.[29] A 2D Perkin Elmer flat-panel detector (model XRD 1621, 2048 × 2048 px, and pixel size of 200 µm) positioned at 1.32 m behind the sample allowed data acquisition of full Debye–Scherrer rings in transmission mode. Measurements were performed with a primary beam height of 10 µm to obtain a satisfactory spatial resolution in the direction of the CG, while the beam width was chosen as 1000 µm for all experiments to obtain the best statistical conditions possible in terms of diffracting domains, as well as keep the measurement time as short as possible. By this means, full diffraction rings were recorded in the range of 0°–12° 2θ angles with an acquisition time of 0.5 s per frame. Additionally, every experiment was repeated to ensure good reproducibility. Since a transmission mode was used, the diffraction volume is integral, and the signal is averaged over the entire 5 mm thickness of the sample.

During the boost steps, the X-ray beam position was consistently maintained 5 to 10 µm below the surface to observe the microstructural changes taking place in the surface region, while during the diffusion steps, continuous vertical scans along the z-direction from the surface down to 500 µm depth were conducted to observe the development of CGs (see Figure 1). During quenching, the X-ray beam position was again kept constant either directly below the surface (around 50 µm below) or at the core (1 mm below), depending on the measurement strategy, as will be detailed in subsequent sections. Upon completion of all processing steps, each sample was scanned at room temperature from the surface to around 1 mm depth with a 20 µm step size.

During the boost and diffusion steps, the temperature remained relatively stable at 930 °C (±3 °C), allowing the laser triangulation system integrated into the hexapod to maintain measurement positions with high precision, up to 10 µm below the surface. However, during quenching, fast temperature changes prevented achieving the same level of precision. Consequently, the data collected during quenching represent an average within the range of about 50 µm to 10 µm below the surface. Despite these variations, they are consistent across all samples and process variations since the cooling rate during quenching is largely uniform, thus not introducing inaccuracies into the comparative analysis of the data.

2.4. Synchrotron Data Evaluation

The collected diffraction patterns were integrated using the Python library PyFAI.[30] In order to determine the detector aberrations and account for the geometrical conditions of diffraction in data integration, 5 mm thick (same as sample thickness) NIST standard LaB6 powder measurements were performed initially using the same setup.[31]

2.4.1. Phase and Carbide Analyses

After the calibration steps, the full 360° azimuthal range was integrated for phase and carbide analyses to achieve the best signal statistic possible. Austenite (γ) and martensite (α′) were the main phases for microstructure analysis, along with various carbides depending on the steel grades. Only austenite (γ) and carbide phases were considered for the boost and diffusion steps at high temperature, while for the quenching step the body-centered tetragonal (BCT) martensite (α′) was added. The diffraction patterns were then evaluated with the convolution-based Rietveld refinement implemented in TOPAS-Academic 6 (Coelho Software, Australia).[32] The Fundamental Parameter Approach[33] integrated in TOPAS was used to analyze the phase fractions and lattice parameters, which account for the emission profile, sample, and instrumental contribution to the diffraction peak profile. Since the process involves a high-temperature range, an isotropic atomic displacement parameter, also known as a temperature factor, was considered and refined in the structure information of each phase in order to elucidate the effect of temperature on the diffraction profile.[34] For all phases analyzed, the temperature parameters were coupled, assuming the same effect for all.

2.4.2. Residual Stress Analyses

Regarding stress generation, the main focus was set on the quenching step with the temporal evolution of stresses in austenite and martensite. For this, the widely applied $\sin^2\psi$ method, involving sample rotation, could not be used. Additionally, continuously changing stresses as well as temperature and composition depth gradients are present in the sample during the entire process, making the determination of the strain-free lattice spacing particularly challenging. Therefore, for the present case, the following justifiable assumptions are made: i) the specimen has no or negligible crystallographic and morphological texture in the measured gauge volume; ii) the composition dependence of the elastic constants is negligible in the measured gauge volume; and iii) a rotationally symmetric stress state parallel to the carburized surface prevails.

For the evaluation of the data, 2D diffractograms were angularly integrated to obtain 72 intensity profiles, with each corresponding to diffraction data from a detector azimuthal segment of $\Delta\delta = 5°$. Subsequently, the martensite {211} and the austenite {311} diffraction lines were fitted with a pseudo-Voigt function to determine azimuthally-dependent lattice spacings $d_\delta^{\{hkl\}}$ using Bragg's law for each of the 72 profiles. The azimuthal dependencies of the lattice spacing, which represent elliptical distortions of the Debye–Scherrer rings, can be directly correlated to (residual) stresses using the elastic constants. The angle $\psi^{\{hkl\}}$ was corrected for

the offset between the scattering vector and the normal of the carburized surface using a simple transformation dependency based on the method provided by Heidelbach et al. and Kurz et al.[35,36] However, this offset is very small due to a high energy of the X-ray beam and the resulting low scattering angles.

After transformation of each of the 72 azimuth angles (δ) to psi angles (ψ), given the preceding assumptions, the relation between the measured X-ray elastic strain ($\varepsilon_{\psi}^{\{hkl\}}$) at different angles ψ and the phase-specific, mechanical stress $\sigma_{xx} - \sigma_{zz}$ are given in Equation (1) (cf. e.g.,)[37]

$$\varepsilon_{\psi}^{\{hkl\}} = \frac{d_{\psi}^{\{hkl\}} - d_{0}^{\{hkl\}}}{d_{0}^{\{hkl\}}}$$
$$\varepsilon_{\psi}^{\{hkl\}} = \left(2S_{1}^{\{hkl\}} + \frac{1}{2}S_{2}^{\{hkl\}}\sin^{2}\psi\right)[\sigma_{xx} - \sigma_{zz}], \text{where} \quad (1)$$
$$S_{1}^{\{hkl\}} = \frac{-\nu^{\{hkl\}}}{E} \text{and} \frac{1}{2}S_{2}^{\{hkl\}} = \frac{1+\nu^{\{hkl\}}}{E}$$

The determined stress direction was longitudinal (σ_{xx}), and the contribution of stresses normal to the surface (σ_{zz}) was not ignored, as the measurements were conducted not only at the surface but also at various depths along the beam height. The temperature dependent macroscopic elastic modulus E and the Poisson's ratio ν were determined based on the macroscopic data published by Richter.[38] These values are extrapolated with polynomial fitting to cover the entire carburizing range. The generated functions for two phases of austenite (γ) and martensite (α') are given from Equation (2)–(5).

$$E^{\alpha'}(T) = 212 - 0.05147 \cdot T - 5,15726 \cdot 10^{-5} \cdot (T)^{2} \quad (2)$$

$$E^{\gamma}(T) = 197.86 - 0.07945 \cdot T \quad (3)$$

$$\nu^{\alpha'}(T) = 0.2847 + 2.8261 \cdot 10^{-5} \cdot T - 4.3296 \cdot 10^{-8} \cdot (T)^{2} + 1.1757 \cdot 10^{-10} \cdot (T)^{3} \quad (4)$$

$$\nu^{\gamma}(T) = 0.2759 + 5.7219 \cdot 10^{-5} \cdot T \quad (5)$$

where T is the temperature in °C. These values are then converted into crystallographic plane-specific constants, called X-ray elastic constants (XEC), using equations presented in literature[39] and used in Equation (1). Subsequently, $d_{\psi}^{\{hkl\}}$- $\sin^{2}\psi$ plots were constructed and the y-intercept of the linear fitting curve was used as strain-free lattice spacing.

All 72 ψ angles, covering full 360°, were used for the determination of residual stresses. The error margins indicated in the figures are the average standard deviation of the four stress values determined from each quarter of the diffraction ring ($\psi = 0°$–$90°$, $90°$–$180°$, $180°$–$270°$, and $270°$–$360°$, see Figure 1a for the position of each quarter).

2.5. Complementary Methods

Subsequent to the in situ investigation, the samples were metallographically prepared for microstructure analyses of the carburized area by using a TESCAN VEGA II XLH scanning electron microscope (SEM) equipped with an Edax Octane Elite energy-dispersive X-ray spectroscopy (EDX) system.

Additionally, EMPA were performed in the carburized region to investigate the elemental distribution. For the EMPA investigations, a JEOL JXA-8200 microanalyzer was used to qualitatively evaluate the chemical distribution of elements. For each measurement, a 0.5 µm step size was adopted, and an area of 300 µm width at carburized surface and 100 µm depth from the carburized surface was investigated with 100 ms per increment.

3. Results and Discussion

3.1. Evolution of Carbon Content During the LPC Process

The evolution of the carbon content throughout the entire process exhibited several common characteristics across all samples and process variations. To avoid redundancy in the following sections, these common observations will be illustrated using a single representative sample. The subsequent sections will then focus on detailing the differences observed between the samples and processes.

A sequence of integrated diffraction patterns of sample LA-20Mn is shown as an example in **Figure 3**.

During the heating, boost, and quench steps, the X-ray beam was consistently positioned directly below the surface (5–10 µm), appearing as a continuous line in the contour plot. In contrast to these steps, during the diffusion, the sample was scanned from the surface toward the depth to monitor the formation of the CG. Individual z-axis scans are noticeable during in the contour plot.

During the initial 10 min heating step, phase transformation can be identified by the disappearance of the α {110} peak and appearance of γ {111} and γ {200} diffraction peaks. Upon contact of acetylene on the hot surface to initiate the boost step, peak shifting occurs rapidly in the initial seconds, followed by a relatively constant peak position until the end of the step, as observed in previous studies.[27,40,41] In the subsequent 22 min diffusion step, seven consecutive scans from the surface to the core were conducted. Each individual scan reveals that the peak position starts at a lower angle and shifts to a higher angle throughout the scan, highlighting the difference in carbon content between the surface and the core. Additionally, by comparing the progression from the initial to the final scan, it can be observed that the initial peak position gradually shifts from a lower to a higher angle, while the final peak position remains relatively unchanged. This indicates that carbon at the surface slowly diffuses into the core, while the carbon content in the core remains nearly constant. This diffusion results in a flatter CG in the final scans, which can be clearly observed by comparing the magnified images of the first and last scans.

During the second boost step, the austenite peaks shifted to lower 2θ angles once again. Similarly to the first boost step, a significant shift occurs within the first few seconds after acetylene entry, with the peak positions stabilizing for the remaining 2 min of the boost step. During the following second diffusion step with nine scans, the austenite peaks gradually shift back to higher 2θ angles, and similarly, the gradient becomes flatter from the initial to the final cycle.

In the last steps of the process, the sample was quenched with high-pressure helium. Strong peak shifting toward higher 2θ angles can be observed in the first seconds due to a higher

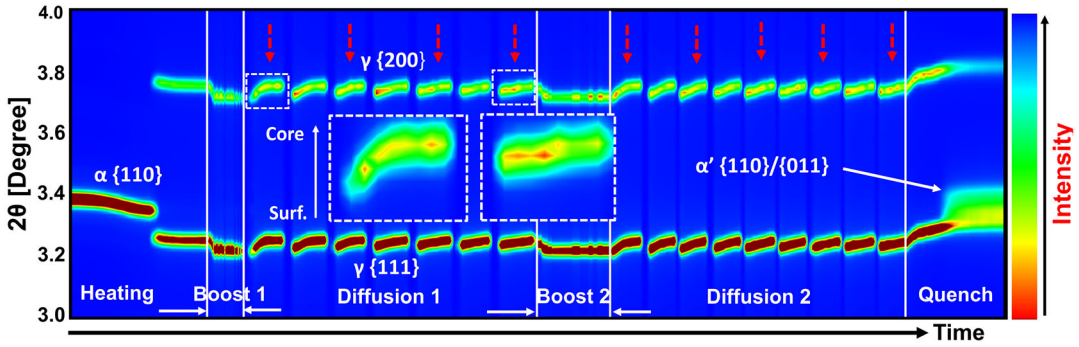

Figure 3. 2D contour plots of integrated diffraction patterns of sample LA-20Mn during the whole process of heating, boost/diffusion cycles and quenching steps. The dashed red arrows mark the individual *z*-axis scans. These scans will be further investigated in the following section to demonstrate the evolution of carbon content depth profiles. Magnification of the γ {200} austenite peak during the initial and the final scans during the first diffusion step are also provided to illustrate the shift in the peak position during scans.

cooling rate at the beginning of quenching, which is followed by a slower, continuous shift of the peaks. The martensitic transformation can also be observed in this step with the appearance of rather broad α′ {110}/{011} diffraction profiles, pointed out with a white arrow in Figure 3 In addition, austenite peaks are still present after quenching, indicating the presence of retained austenite.

Observation of peak shifting toward lower and higher 2θ angles is an indication of the change in lattice distances. After integrated diffraction patterns were analyzed, the evolution of the lattice parameter of austenite and martensite was determined. From the lattice parameter of austenite, the change of carbon content was then calculated by using the model developed by Onink, taking into account the thermal effect as given in Equation (6).[42]

$$a_\gamma = (0.363067 + 0.000783x_C^r) \cdot [1 + (24.92 - 0.51x_C^r) \cdot 10^{-6} \cdot (T - 1000)] \quad (6)$$

Here, x_C^r is at% carbon, and T is the temperature in Kelvin. **Figure 4** details the change of the average carbon content dissolved in austenite during the first and the second boost/diffusion cycles for the sample LA-20Mn. The specific HEXRD scans during diffusion are also highlighted in the 2D contour plot (Figure 3) by red dashed arrows.

During the first boost steps (Figure 4a gray line), the calculated carbon content increases sharply during the initial 10 s and approaches, or potentially slightly exceeds, the solubility limit of the steel, 1.28 mass%. Subsequently, despite the continued presence of acetylene in the chamber, the carbon content decreases slightly to around 1.2 ma%. The large CG built-up in the material during the boost step leads to a very high diffusion potential between the surface and the core. In the following diffusion step, this large gradient can be seen in the first scan after 3 min, where the carbon content at the surface is around 1.13 ma% and sharply reduces over 150 µm in depth, forming the CG. However, after 8 min of diffusion, the carbon content at the surface reduces to around 0.8 ma%, while it increases in depth up to about 300 µm due to diffusion. The diffusion rate is notably faster during the first scan of the diffusion step compared to subsequent scans, which is due to the higher driving force created by the accumulation of carbon at the surface. At

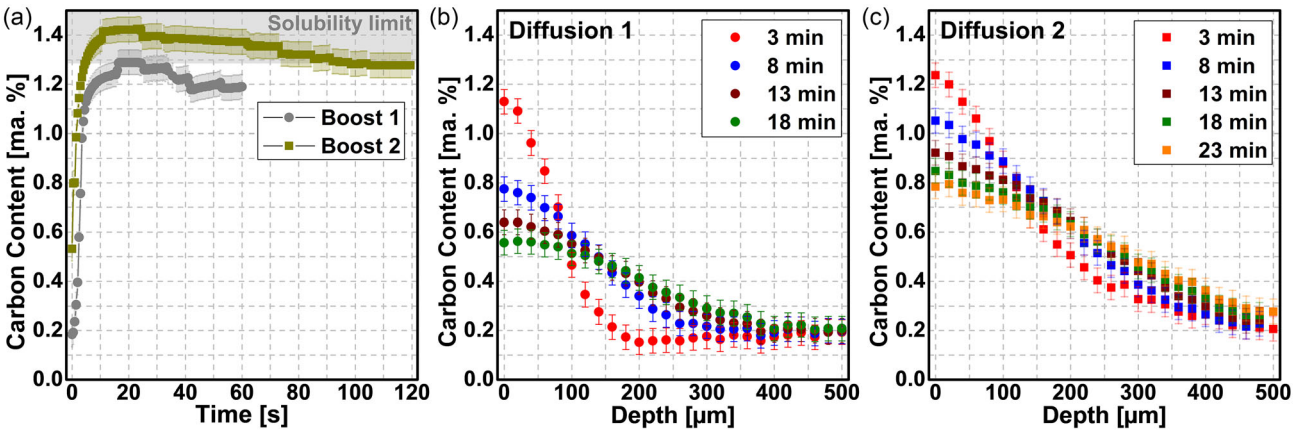

Figure 4. Evolution of carbon content in austenite: a) during the boost step at the sample surface, b) during scanning from the surface to the core during the first diffusion step, and c) the second diffusion for sample LA-20Mn. Diffusion scans shown in (b) and (c) corresponds to the scans marked with red arrows in Figure 3, where the first scan represents the 3rd min.

the end of the first diffusion step, the carbon content at the surface reaches around 0.56 ma%, while at a depth of about 500 µm the nominal carbon content of 0.2 ma% is still maintained.

During the second boost step, the calculated carbon content initially appears to rise above the solubility limit of austenite, following a pattern similar to that observed in the first boost step. However, the solubility limit is reached more quickly in this cycle, and the carbon content remains above the solubility limit until the end of the boost step, despite the ongoing decrease. In the following diffusion step, the CG continues to form into the depth, as already observed in the first cycle. Since a gradient was established during the first cycle, the diffusion rate during this step is of a comparable magnitude to that observed previously, that is, the change in gradient during the second boost step between each scan is less apparent than that observed during the first boost step. This indicates a more consistent diffusion rate among each of the diffusion scans compared to the initial diffusion step.

One of the main observations was the calculation of carbon content beyond the solubility limit of austenite during both boost steps. The underlying reason for this could be the oversaturation phenomenon of austenite for a short duration, induced by a rapid influx of carbon that creates a temporary nonequilibrium state.

Another significant observation during the boost steps was the decrease of the carbon content after saturation, despite the continuous supply of the carbon-donor gas. This suggests that carbon diffusion begins almost immediately as the boost step starts. The observed reduction in carbon content below the solubility limit indicates that the surface cannot effectively absorb additional carbon after the initial surge. This phenomenon is attributed to the possible carbide formation at the surface, hindering the further acetylene decomposition or absorption. Consequently, this reduces the carbon intake of the surface, although acetylene is still present. This effect was more pronounced in the first boost step, where the CG was steeper, creating a stronger driving force for diffusion. As a result, the carbon content drops more sharply after saturation compared to the second boost step, where the gradient is less steep and the driving force for diffusion is weaker.

The final point that can be noticed during the boost step is the stepwise decrease of the carbon content, which is caused by the surface adjustment of the hexapod. As indicated previously, the beam was adjusted around 5 to 10 µm below the carburized surface during the boost steps, averaging the carbon content in the measured height (10 µm beam height). During the process, variations in temperature with magnitudes of up to 10 °C, were observed particularly at the points where the atmosphere is changed between vacuum and acetylene. These changes in temperature caused a thermal expansion or contraction of the system, shifting the sample slightly above or below the beam position. This was continuously corrected with a 10 s delay by the laser triangulation distance measurement system connected to the hexapod. The effect of these corrections created incremental changes of the determined values, as shown in the boost steps graphs in Figure 4. At steep CGs, this corresponds to an apparent variation of $\approx\pm$ 0.03–0.05 ma%. While clearly detectable, this artifact does not affect the interpretation of the diffusion kinetics, solubility limit exceedance, or carbide formation/dissolution trends.

The above-mentioned carbide formation during the boost steps was further analyzed by Rietveld refinement of the in situ diffraction data and by complementary EMPA analyses after the end of the process. **Figure 5** presents diffractograms of respective time frames belonging to the first boost and diffusion cycle. The peaks are positioned with an offset from bottom to top, starting from the early seconds of each boost step to the respective minutes of the following diffusion steps.

During the initial 10 s of the first boost step, no indication of carbide formation can be observed since the solubility limit was not reached yet, so it can be assumed that the amount of carbon that can be dissolved in austenite was still continuously increasing. After reaching the solubility limit, carbides start to form and small carbide peaks can be identified close to the first austenite peaks in the diffraction pattern after 20 s, and they continue to grow until the end of the boost step. Based on the Rietveld analyses, potential carbides are M_3C, M_6C, M_7C_3, and $M_{23}C_6$, where M is iron, chromium, and/or manganese. Among these, M_3C (in 2θ 2.85°, 3°, 3.06°, 3.3°, 3.36°, 3.44°, 3.6°, and 3.66°) contributes most significantly to the observed peaks, followed by M_6C (in 2θ 3.06°, 3.3°, and 3.44°). Due to the structural similarities among these carbides, distinguishing their peaks is challenging. However, given that the identified carbides only form during the boost step and dissolve within ≈10 min of the diffusion step, they are

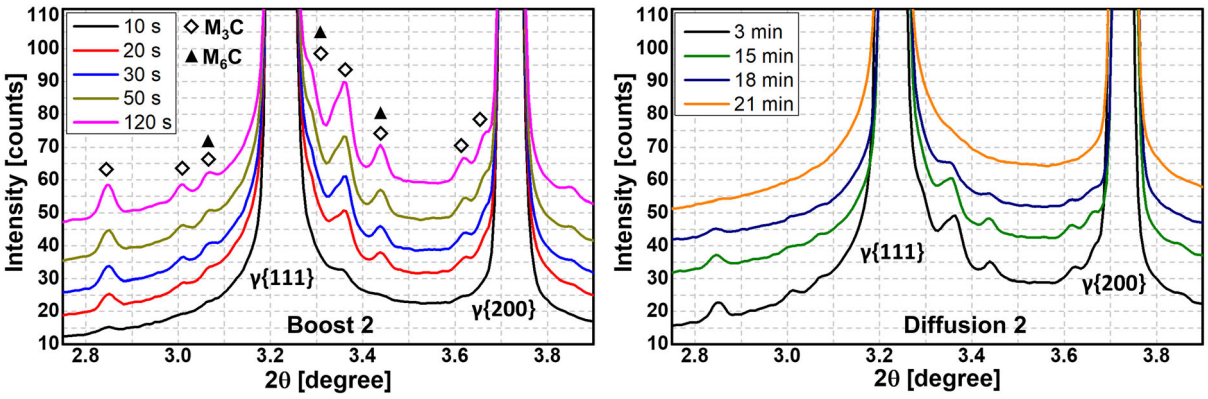

Figure 5. Carbide formation and dissolution during the first boost and diffusion steps near the main austenite peaks of sample LA-20Mn. An offset of +10 counts was applied by taking the first diffractogram as a reference for visualization purposes.

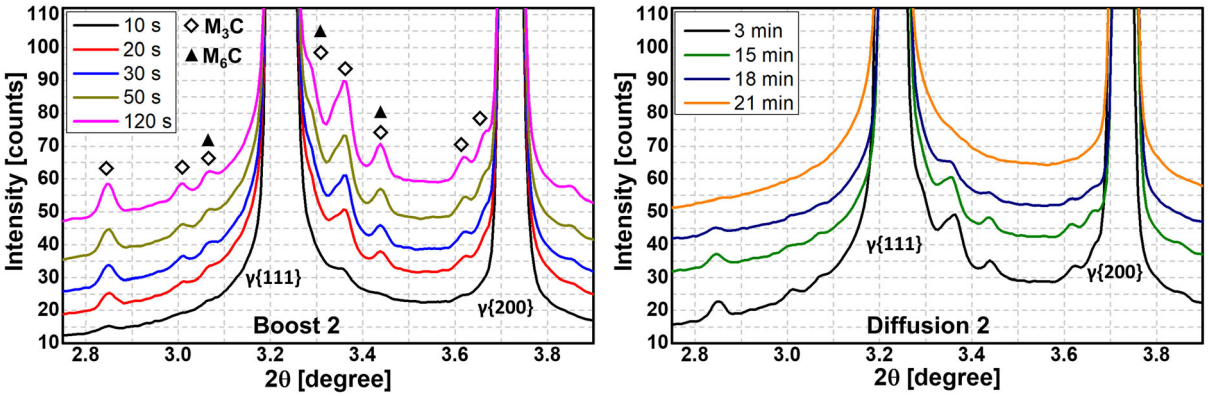

Figure 6. Carbide formation and dissolution during the second boost and diffusion steps near the first austenite peaks of sample LA-20Mn. An offset of +10 counts by taking the first diffractogram as a reference was applied for visualization purposes.

most likely predominantly unstable Fe_3C (cementite), with possible substitution of Fe with Cr and/or Mn atoms.

When the acetylene flow is stopped at the end of the boost step, carbides start to dissolve gradually in the following diffusion step. After ≈6 min of diffusion, low-intensity carbide peaks are still identifiable. After around 9 min, all carbides in the gauge volume are dissolved and the peaks disappear.

The carbide formation behavior observed for sample LA-20Mn in the second boost step is largely similar to that observed in the first boost step in terms of carbide formation and dissolution durations, as illustrated in **Figure 6**.

Upon reaching the solubility limit of austenite, carbides start to form and remain present until the conclusion of the boost step. In contrast to the first boost step, small carbide peaks are already detectable after around 10 s, indicating that the solubility limit is reached earlier than during the first boost shown in Figure 4. In the subsequent diffusion step, carbides start to dissolve gradually. Full dissolution of carbides can only be achieved after around 21 min, which is substantially longer than in the first diffusion step. This observation emphasizes the necessity to extend the duration of the diffusion step in proportion to the duration or number of boost steps, as the time required for complete carbide dissolution increases with each successive boost step.

At the end of the two boost-diffusion cycles, samples were quenched with high-pressure helium ($T_{8/5} = 9$ s) in order to achieve the desired martensitic structure. **Figure 7** gives the phase changes and the cooling curve of sample LA-20Mn during quenching.

The high carbon content at the surface of the sample stabilized the austenite, delaying any phase transformation until the martensite start temperature (M_s) is reached during cooling. As depicted in the graph, the determined martensite start temperature is 195 °C. Based on the experimentally determined M_s temperature, the carbon content dissolved in austenite prior to quenching can be determined using the empirical equation developed by van Bohemen.[43] The model aims to calculate M_s of steels having 0.1–1.9 ma% C and less than 7 ma% of other alloying elements. According to the model, M_s can be formulated as

$$M_s = 565 - \sum_i K_i x_i - 600[1 - \exp(-0.96 x_C)] \quad (7)$$

where x_C is the amount of carbon in ma% and $\sum_i K_i x_i = 31x_{Mn} + 13x_{Si} + 10x_{Cr} + 18x_{Ni} + 12x_{Mo}$ describes the contribution of other substitutional elements. Applying the equation, a carbon content of about 0.76 ma% dissolved in austenite can be estimated for M_s of 195 °C. This value correlates well with the 0.78 ma% carbon content estimated by the lattice expansion close to the surface at the end of the second diffusion step (see Figure 4). Since the final scan given in Figure 4 is from the 23rd min of the 25 min diffusion step, this difference is expected to be even lower after the diffusion of carbon within the remaining 2 min.

Additionally, the carbon content in solution in the tetragonal martensite can be assessed based on the lattice parameters. A linear relationship between the tetragonality and the carbon content in martensite exists according to Equation (8).[44]

$$c/a = 1 + 0.0443 x_C \quad (8)$$

where c and a are the lattice parameters of martensite and x_C is the amount of ma% carbon dissolved in martensite. Other

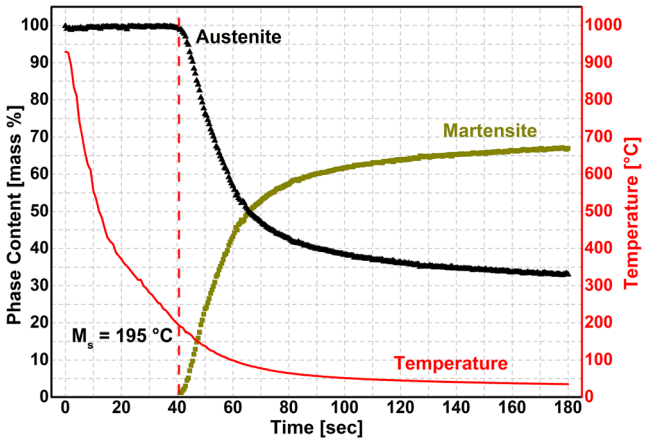

Figure 7. Evolution of the phase fractions of sample LA-20Mn during quenching from the austenite region.

alloying elements, such as chromium and manganese, substitute iron, so they only have a minor effect on the c/a ratio of martensite. Moreover, the tetragonality ratio is independent of the temperature, since both the a and c lattice parameters of martensite are affected in exactly the same way by the temperature. The evolution of the determined lattice parameters as well as the calculated carbon content dissolved in martensite is presented in **Figure 8**.

In the early stages of transformation, the measured lattice parameters display high standard deviations due to a low amount of transformed martensite. During the first 5 s, until the temperature reaches 170 °C, the lattice parameter c increases sharply and then gradually decreases, while the lattice parameter "a" shows a gradual constant decrease during the transformation.

The tetragonality of the martensite, expressed as the c/a ratio, increases during the transformation, meaning that the first 9% of martensite formed in the first 5 s has a very low c/a ratio compared to later-formed martensite. This might be due to phase-specific second-kind hydrostatic compressive stresses generated at early stages of transformation because martensite formed at early stages is a minority phase. As the transformation progresses and martensite becomes the dominant phase, the compressive stresses reverse, resulting in a higher c/a ratio. A similar phenomenon has been reported in previous studies.[45,46]

Another possible reason for the lower c/a ratio in the early stages of the transformation might be the lower carbon content of fresh martensite formed in the high-temperature range. Before quenching, there might be some prior austenite regions that have slightly lower carbon content than the majority ones, causing them to transform earlier due to their higher M_s temperature. This may also be an indication that carbon atoms were not evenly distributed in the gauge volume during the diffusion steps. Although carbon atoms had sufficient time and temperature for homogeneous distribution, some of the carbides that dissolved later during the final diffusion step might leave some carbon agglomerates in austenite, creating local inhomogeneities.

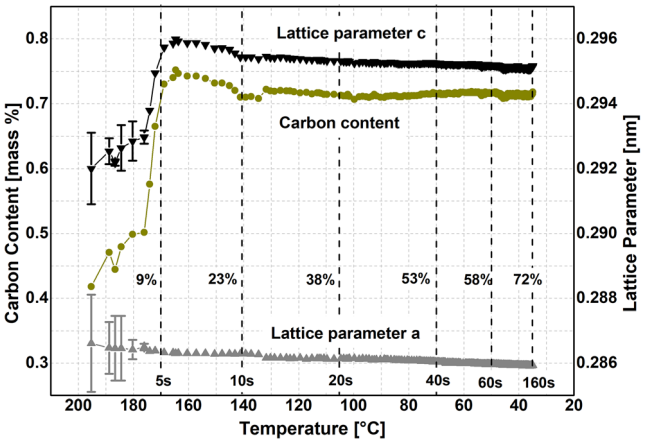

Figure 8. Evolution of the lattice parameters of martensite and the calculated carbon content in solution for sample LA-20Mn as a function of temperature. Dashed vertical lines show the time from the beginning of martensitic transformation in seconds and ma% of the transformed martensite.

Furthermore, the carbon content calculated via Equation (8) at the end of quenching is about 0.72 ma%, which is slightly lower than the surface carbon content (0.78 ma%) determined in austenite at the end of the boost step. One reason for this can be attributed to self-tempering and/or carbon partitioning from martensite during quenching, as expected and observed in literature.[47–49] As the diffusion coefficient is still high in the early stages below M_s, self-tempering through segregation of carbon atoms to lattice defects is still probable.[50]

3.2. Effect of Acetylene Amount on the Evolution of Carbon Content

The effect of acetylene supply during the boost steps on the evolution of the carbon content was investigated by doubling the boost step duration for two different steel grades, for 20MnCr5 and for Pyrowear 53, as shown in Table 2.

Figure 9 details the evolution of carbon content during the first boost-diffusion cycles of 20MnCr5 for lower and higher amounts of acetylene supply, designated as LA-20Mn and HA-20Mn, respectively. A sharp increase of the carbon dissolved in austenite is evident in the early seconds of the boost steps with the same rate of increase, which agrees with previous observations. During the first boost steps, the carbon content in both samples rises to ≈1.3 ma% before gradually decreasing until the end of the step, where no obvious effect of a longer boost step duration can be observed.

As mentioned earlier, a supposedly stepwise decrease or increase of the carbon content during the boost step is caused by the correction of the gauge volume position within the sample by the active height compensation (triangulation measurement plus height compensation by means of the hexapod). Due to the rather steep CG, even a 10–15 µm change of beam position causes a distinguishable effect on the determined carbon content.

Carbon content depth profiles of both samples in the early minutes of the diffusion steps are also very similar. However, towards the end of the diffusion step, around 12% higher carbon content is observed in the near-surface region of the HA samples compared to the LA samples. During the subsequent boost step, the carbon content in the near-surface region of both samples increases to almost similar levels. Nonetheless, the disparity in carbon content at higher depths continues to widen. By the end of the second diffusion step, the HA sample exhibits higher overall carbon content around 18%, throughout the depth profile.

Although the carbon content reaches nearly comparable levels after the boost steps in both conditions, the accumulated carbon at the surface, along with potentially formed carbides, contributes more significantly to the overall carbon content in the HA sample. This results in ≈18% higher total carbon content throughout the depth profile. This indicates that the primary effect of the increased acetylene concentration is to enhance surface carbon accumulation and carbide formation during the boost step, which subsequently influences the final carbon content during the diffusion step, if the required diffusion time is given.

Figure 10 shows the evolution of the carbon content for the same process parameters repeated for the Pyrowear 53 steel

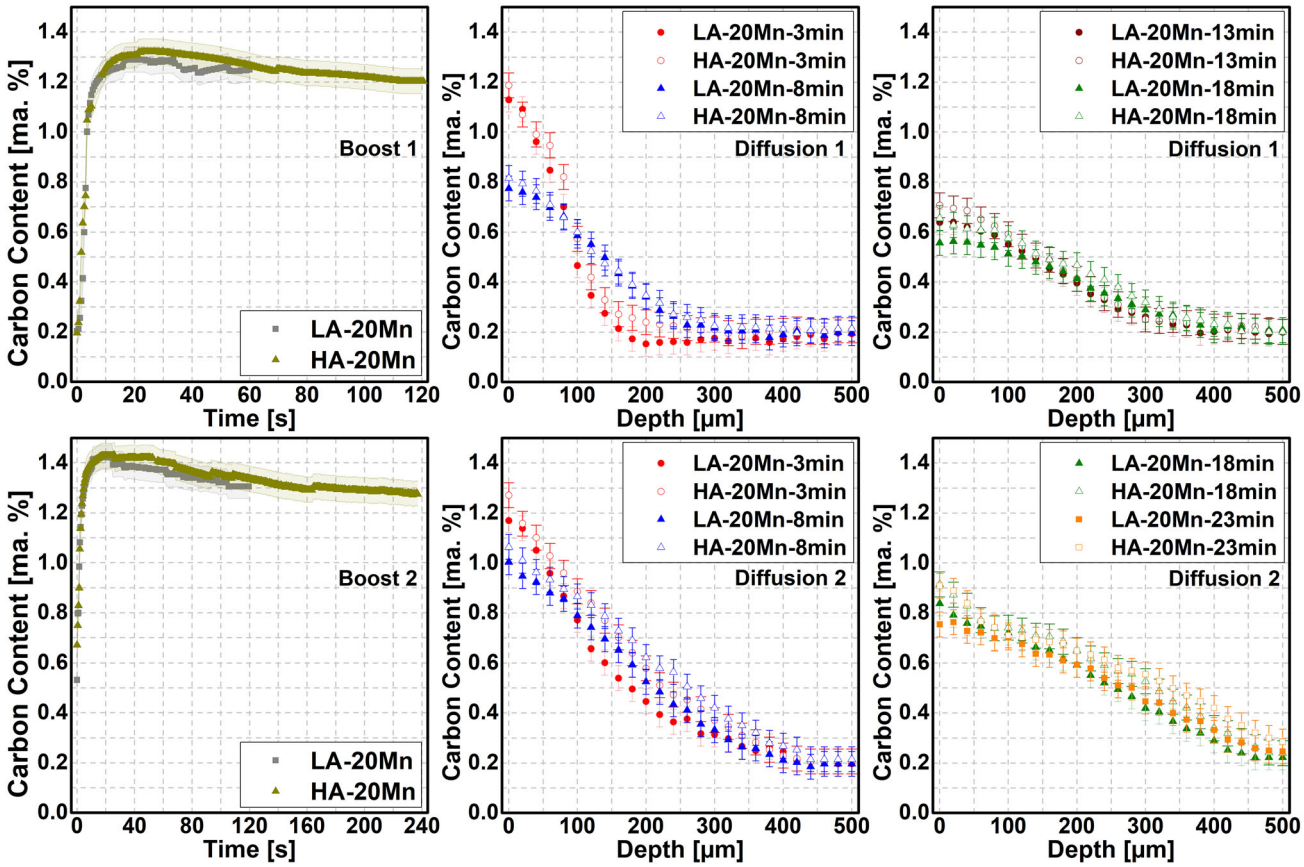

Figure 9. Evolution of carbon content during the boost and diffusion steps of 20MnCr5 samples carburized with different boost step durations.

grade. The overall behavior of this steel is similar to that of steel grade 20MnCr5. However, it can be noticed that the carbon content increases during the boost step up to around 1.2 ma% for both samples instead of 1.3 ma% as observed for the steel grade 20MnCr5. The reason for this is attributed to the higher molybdenum and chromium content, which are ferrite stabilizers, in combination with a lower initial amount of carbon and manganese, which are austenite stabilizers. As a consequence, the austenite field decreases and its solubility limit is shifted to lower values.

For the Pyrowear 53 grade, the evolution of the carbon depth profile during diffusion exhibits a behavior similar to that of the 20MnCr5 grade. Notably, in the near-surface region, the HA sample shows a higher carbon content compared to the LA sample, which becomes more pronounced during the second diffusion step. It has to be remarked, that several parameters can influence the carbon uptake and diffusion, in particular grain size and lattice defects,[51] which should be considered when directly comparing different alloys and conditions.

3.3. Carbide Formation at the Surface During Boost Step

One major focus point of the study was the formation of carbides during the boost step. The effect of carbide-forming elements on the carburizing process is often reported in literature, mostly related to the effect of carbon atom consumption in austenite by carbide precipitation.[52,53] During carburizing at full austenitizing temperatures, in addition to the carbon atom consumption effect, carbide-forming elements not only reduce the diffusivity of carbon by decreasing the diffusion coefficient and increasing the diffusion activation energy,[54] but also form carbides perpendicular to the carbon flux direction, which can act as a physical barrier.[55] Furthermore, as acetylene is a catalytically decomposable hydrocarbon, which requires an active metal catalyzer surface,[56] the decomposition reaction slows down in contact with intermetallic carbides.[8]

To investigate the extent of the mentioned effects on carbide formation in the different steel grades, experiments with direct quenching after 5 min of boost were designed (see Table 2). This allowed to retain the carbides at the surface as much as possible. At room temperature, measurements were performed at the surface region. **Figure 11** presents the X-ray diffractograms of the steel grades examined at room temperature before and after the treatment at process temperature.

As expected, the higher carbon content, combined with the presence of austenite-stabilizing elements, resulted in a significant amount of retained austenite. This is evident from the higher intensity of the γ {111} austenite peak compared to the α′ {110}/{011} martensite peak.. The 14NiCrMo13-4 steel grade exhibited the highest amount of 94 ma% retained austenite, followed by Pyrowear 53 with 92 ma%, 18CrNiMo7-6 with 91 ma%, and 20MnCr5 with around 84 ma%. The three steel grades

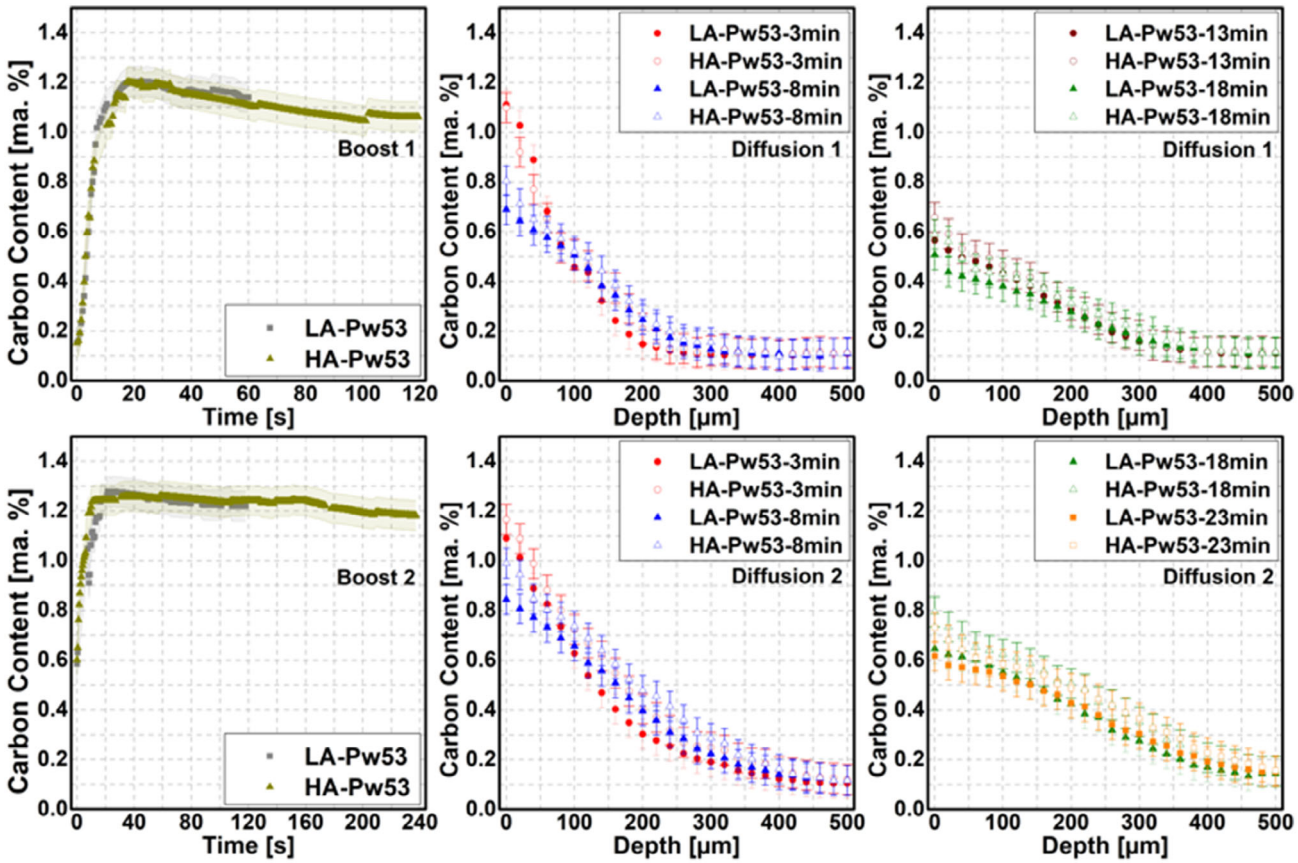

Figure 10. Evolution of carbon content during boost and diffusion steps of Pyrowear 53 samples carburized with different boost step durations.

20MnCr5, 14NiCrMo13-4, and 18CrNiMo7-6 exhibit rather similar carbide peaks near the austenite γ {111} peak after the boost step due to their comparable elemental compositions. Similar to Figure 5 and 6, the identified carbides are mainly in the form of Fe_3C, with a possible contribution of M_6C. Among the three steel grades, 20MnCr5 and 14NiCrMo13-4 show no carbide presence in the initial state, while 18CrNiMo7-6 exhibits some carbides. These are most likely Cr carbides in the form of M_3C, attributable to the higher chromium content in this steel grade.

Given the higher concentration of carbide-forming elements, particularly molybdenum, Pyrowear 53 exhibited significantly more intense carbide peaks in both the initial state, and of course, after treatment. The effect of alloying element content on the peak intensities is most apparent for carbides growing at the 2θ angles of about 3.05°, 3.22°, and 3.52°, which could be attributed to the contribution of stable molybdenum-rich M_6C and M_3C carbides, as these carbides are also present in the initial state. Another observation was the low intensity of the carbide peak at the 2θ angle of about 2.88° for Pyrowear 53 steel compared to the other three grades. Considering that this peak is probably originating from Cr-rich carbides as is most apparent for the grade 18CrNiMo7-6 steel due to its higher Cr content, this observation is also expected due to the lower Cr and Mn content of the Pyrowear 53. Although the carbide identified mainly is in the form of M_3C, different intensities of the peaks suggest the contribution of alloy carbides. The observed correlation of Cr and Mn contents, and the intensity of the corresponding peaks for all steel grades also support this result.

Figure 12 shows the results of complementary EMPA measurements of the four steel grades performed after a 5 min boost step followed by direct quenching. The red color signifies areas with carbon concentrations exceeding the equilibrium solubility limit, achieved by normalizing the carbon content based on the theoretical solubility limit of each steel.

For all steel grades, a pronounced accumulation of carbon is apparent at the surface. These accumulations, which exhibit distinct pathways toward the depth, being higher in certain areas compared to others at the same depth, suggest that carbides accumulate at grain boundaries. This effect is more pronounced in 20MnCr5 and 18CrNiMo7-6 steel. After 5 min of diffusion, the highest carbon penetration depth is reached in the 20MnCr5 steel. Steel grades 14NiCrMo13-4 and 18CrNiMo7-6 exhibit similar carbide formation behavior at the surface, with 18CrNiMo7-6 displaying ≈10 µm deeper penetration. This outcome is rather unexpected, as 18CrNiMo7-6 contains higher concentrations of carbide-forming elements, such as chromium and molybdenum, which are expected to slow down the diffusion of carbon. The reduced carbon penetration in 14NiCrMo13 is attributed to its lower base carbon content compared to 18CrNiMo7-6, which may affect the time required to reach the solubility limit, particularly in regions farther from the surface. Despite having the lowest theoretical solubility limit, Pyrowear 53 exhibits the

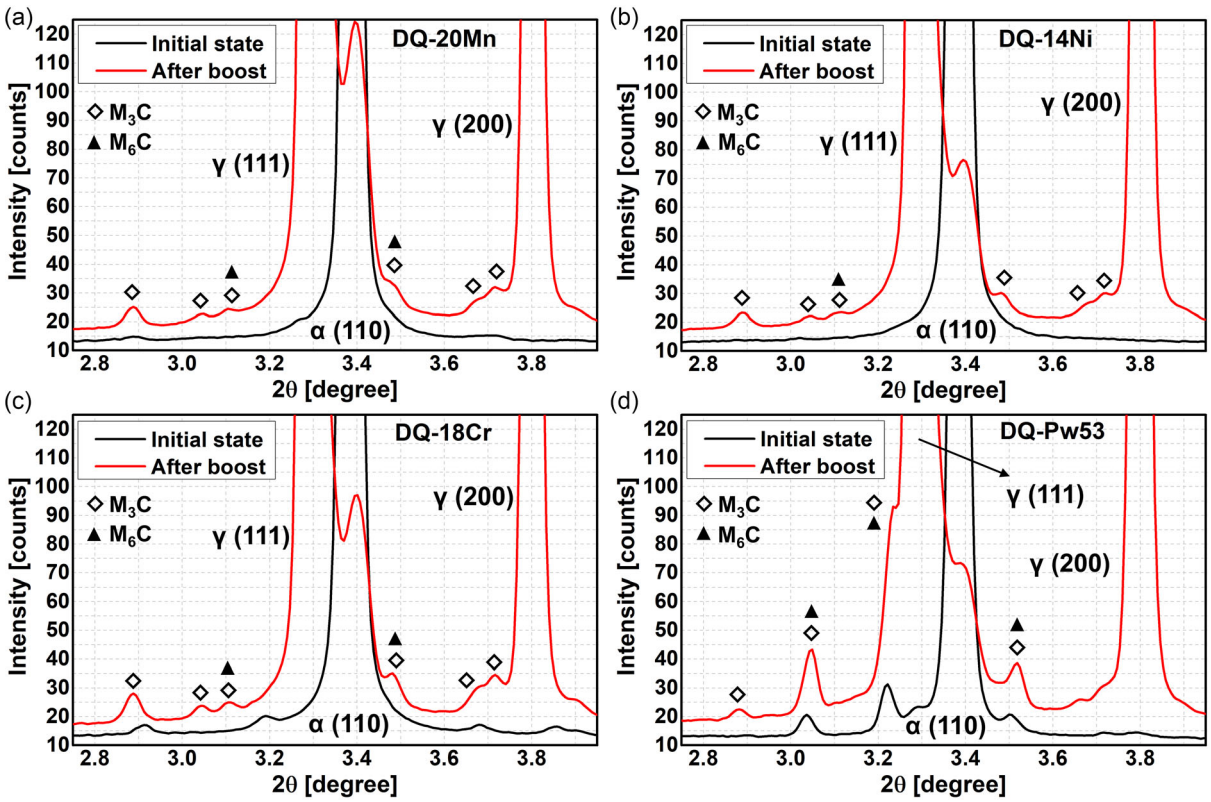

Figure 11. X-ray diffractograms showing carbides for four different steel grades at room temperature in initial state before LPC and after 5 min of continues boost followed by direct quenching: a) 20MnCr5; b) 14NiCrMo13-4; c) 18CrNiMo-7-6; d) Pyrowear 53. An offset of +10 counts by taking the first diffractogram as a reference was applied for visualization purposes.

shallowest carbon penetration depth, while significant carbon accumulation is observed at the surface.

As mentioned previously, differences in carbide amounts are primarily attributed to the effect of carbide-forming elements, which reduce acetylene decomposition and carbon diffusion by acting as a barrier. In order to observe this effect more quantitatively, the 2D maps shown in Figure 12 are integrated into 1D CG profiles for given steels. The results of the integration are presented in **Figure 13**.

The areas under each curve, which represent the total amount of carbon in solid solution and in the form of carbide for each steel grade, were calculated as 836, 940, 954, and 772 units (μm × carbon content) for the steel grades 14NiCrMo13-4, 20MnCr5, 18CrNiMo7-6, and Pyrowear 53, respectively. Total carbon intake for 20MnCr5 and 18CrNiMo7-6 are very similar, indicating that the supplied carbon in these steels contributes to the overall CG by either dissolving in austenite or forming carbides. However, the values for 14NiCrMo13-4 and Pyrowear 53 are lower compared to the first two grades. The difference observed for 14NiCrMo13-4 can be partially attributed to the lower initial carbon content, while the difference of Pyrowear 53 suggests that carbon uptake is likely hindered by the formation of the carbide layer at the surface.

Due to variations in the diffraction peak intensities for the Pyrowear 53 steel grade, further carbide analysis was conducted using EDX in the surface region. **Figure 14** shows an SEM image of the near-surface area along with corresponding EDX data. The EDX data indicate that carbides formed near the surface during the boost step are primarily iron carbides with additions of Mo and Cr, whereas the Mo-carbides were observed at larger distances from the surface, likely originating from the base material prior to the heat treatment.

3.4. Carbide Dissolution

The carbide dissolution behavior can also be investigated by comparing the diffusion steps of LA samples (see Table 2). **Figure 15** shows the X-ray diffractograms at the surface of the sample during the diffusion steps for 18CrNiMo7-6 and Pyrowear 53. Similar to the behavior of the LA-20Mn sample given in Figure 6, carbides formed during the second boost step of LA-18Cr almost completely dissolved after about 9 min of diffusion as shown in Figure 15a. By the 21st min of the diffusion step, no detectable carbide peaks can be observed in the sample. The same carbide dissolution behavior is seen for the LA-Pw53 sample, where the carbide peaks at the 2θ positions of about 2.85°, 3.38°, 3.61°, and 3.62° gradually disappear. Consistent with previous observations, the dissolution behavior suggests that the carbides observed in LA-18Cr are mainly cementite and possibly, to some extent, chromium-rich M_6C, which are rather unstable at high temperatures.[57–59]

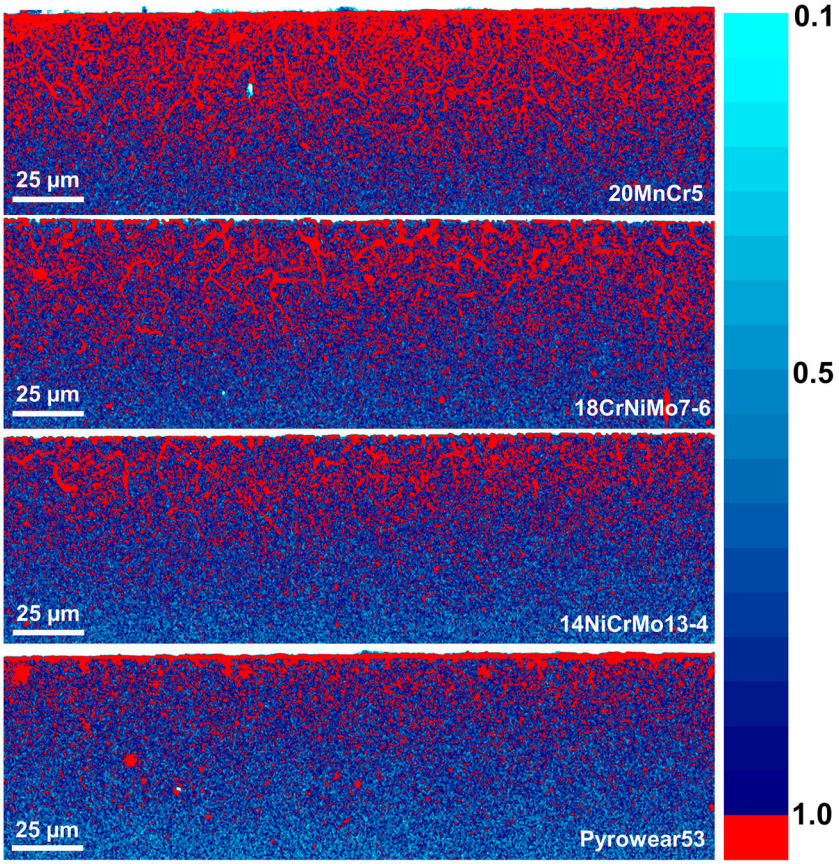

Figure 12. EMPA measurement showing surface carbon accumulation after a 5 min boost step followed by direct quenching for examined steel grades. The color scale, ranging from light blue to dark blue, is normalized based on the theoretical solubility limit of each steel at 930 °C. These solubility limits are set at 1.28 ma%, 1.32 ma%, 1.26 ma%, and 1.22 ma% for DQ-20Mn, DQ-18Cr, DQ-14Ni, and DQ-Pw53, respectively. Red colored regions indicate areas with carbon concentrations exceeding the equilibrium solubility limit.

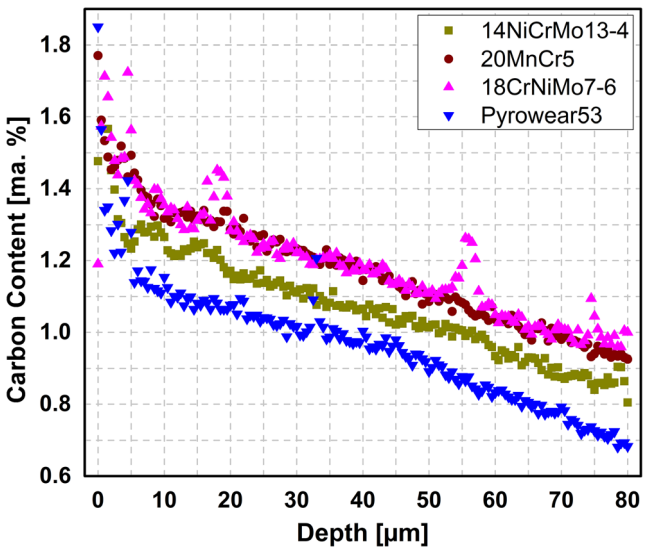

Figure 13. Integrated carbon depth profiles from 2D EMPA results (cf. Figure 12) for the four different steel grades.

On the contrary, for the LA-Pw53 sample, carbides formed at the 2θ angles of about 3° and 3.47° remain almost unchanged throughout the diffusion step. This is attributed to the cementite-stabilizing effect of molybdenum[60] and the strong contribution of molybdenum-rich M_3C and M_6C carbides on peak intensities, as these are the dominant compounds of the carbides at high temperature and, depending on the other alloying elements, require a temperature of more than 1000 °C for full decomposition or dissolution.[61,62]

3.5. Stress Evolution During Quenching

As is well known, the amount of carbon dissolved in austenite before quenching affects the M_s temperature, and through the martensite transformation, stresses develop during quenching. Through LPC the carburized samples exhibit a gradient of M_s temperatures linked to the carbon content profile. This phenomenon, combined with the temperature gradient from the surface to the core during quenching, creates a distinctive stress evolution, which depends on this transformation sequence. During cooling, the sample surface will experience a higher cooling rate compared to the core, but it will also have a lower M_s temperature

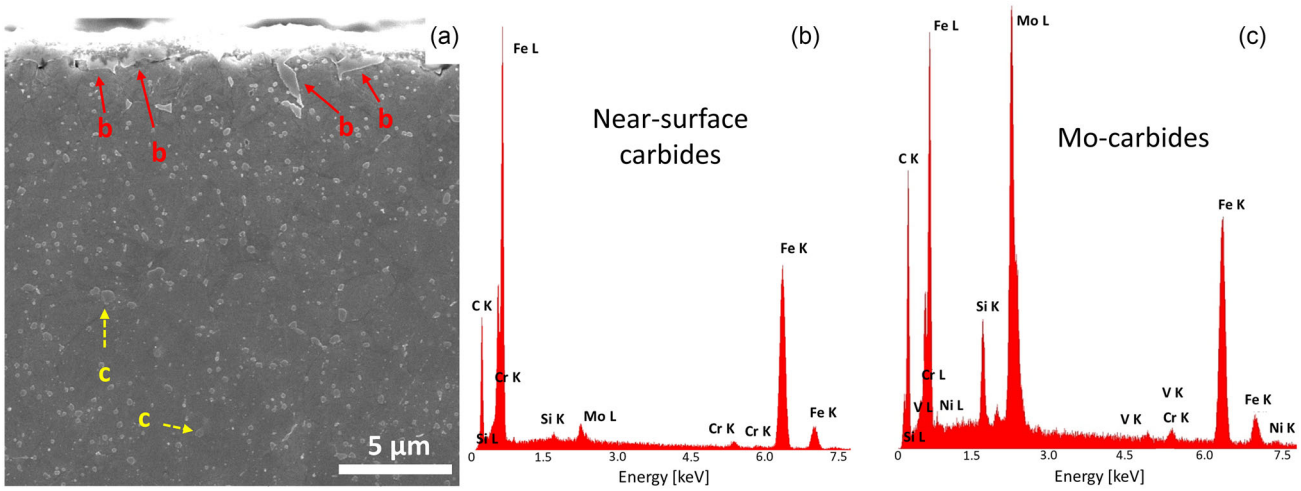

Figure 14. a) SEM image of the near-surface region showing carbides. b) Representative EDX data of near-surface carbides marked with red arrows and c) Mo-carbides below the surface shown with yellow dashed arrows.

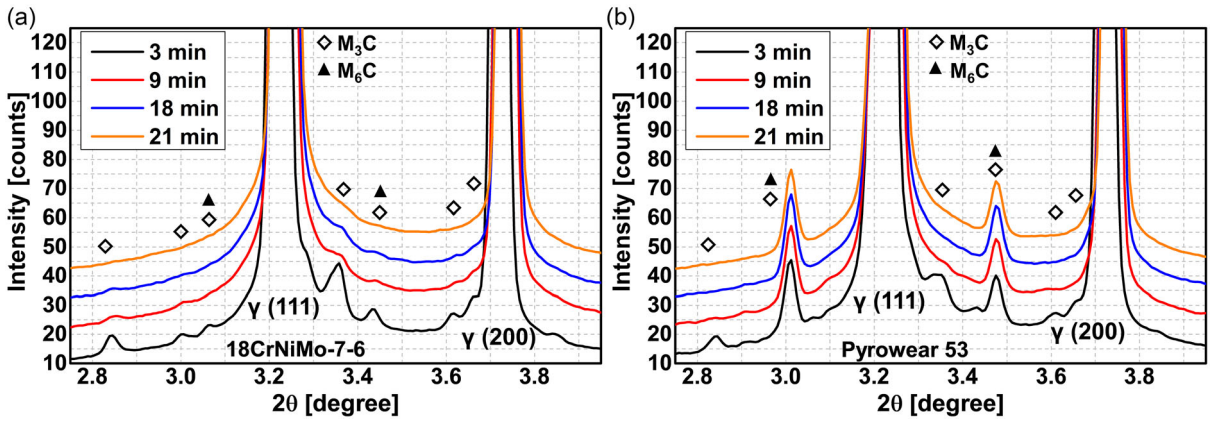

Figure 15. Carbide dissolution during the second diffusion steps of samples LA-18Cr a) and LA-Pw53 b). An offset of +10 counts was applied for visualization purposes.

due to the higher carbon content. As a result, the austenite at the surface will transform much later than the core, contrary to what is observed in steels that have a homogeneous elemental distribution, that is, in total, a rather complex interdependence is present.

In this section, the evolution of stresses during quenching will be addressed and compared for the three different steel grades—20MnCr5, 18CrNiMo7-6, and Pyrowear53—for the carburizing conditions with a LA process (designation LA). The evolution of stress in the 14NiCrMo13-4 grade is not discussed, as its carbon content evolution remains within the range of the other steel grades (see Figure 13), and consequently, its stress evolution also falls within this range. Additionally, since the amount of carbides was very low compared to the measured volume, their effect on the evolution of stress for Pyrowear 53 steel was considered negligible and thus ignored. For the other steel grades, the carbides had already dissolved below the detection limit, and it was therefore assumed that they had no impact on stress evolution.

Figure 16 shows the carbon depth profiles of steels after carburizing determined from the XRD results by using Equation (6) as already presented in the previous sections. **Figure 17** details the evolution of longitudinal stresses ($\sigma_{xx} - \sigma_{zz}$), that is, the stress component parallel to the surface (cf. Figure 1a) in both phases of austenite and martensite for the three steel grades examined. The evolution of stresses at the surface and in the core (1 mm below the surface) is given, while transformation points during quenching are indicated for 18CrNiMo7-6 in Figure 17a. For 20MnCr5 and Pyrowear 53, only the evolution of the stresses at the surface is presented, since core values are similar for all steel grades investigated here.

As the core cools slower than the surface, a lower specific volume of the surface creates around 50 MPa thermal stresses in tension during the early stages of quenching, as shown in Figure 17a for the 18CrNiMo7-6 sample. These tensile stresses are compensated for by compression stresses in the core. Subsequently, at around 380 °C, a strong further increase of

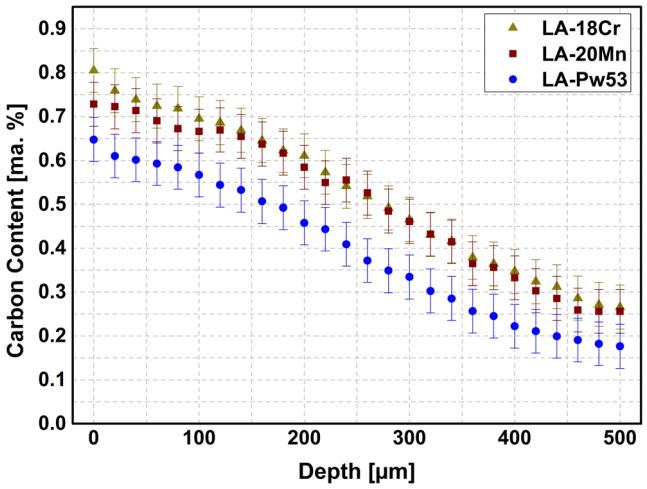

Figure 16. Carbon depth profiles of three different steel grades carburized using the same process variation directly after the second diffusion step, before quenching.

the tensile stresses up to around +250 MPa can be observed at the surface for austenite. This temperature is very close to the start of the martensitic transformation of the core, which, according to the nominal composition of the steel and through Equation (7), has an estimated M_s of 396 °C. This indicates that the core transformation is indeed the main cause of the tensile stresses observed at the sample surface and can be explained as follows. During quenching, the transformation of the core precedes which results in an expansion of the specific volume of the core. This expansion is not fully compensated by the still-soft austenite at the surface, leading to further tensile stress in the austenite phase at the surface. Between 400 °C and ≈170 °C, the tensile stresses in austenite in the near-surface volume continue to rise, reaching around +350 MPa, which is close to the yield point of the material at this temperature. However, around 170 °C, a turning point occurs, which corresponds to the approximate martensitic transformation temperature reached at the surface. This transformation also induces a volume increase; however, this expansion is restricted by the already hardened, rigid core. Thus, tensile stresses in austenite at the surface gradually reduce and invert to a compressive state. For the newly formed martensite at the surface, the first data point shows compressive stresses of around −300 MPa, which then decrease to 0 MPa in the following 0.6 s (2–3 data points) subsequently increase again up to around −250 MPa during the later stage of the transformation. In the core, a compressive stress state of around −80 MPa forms at the beginning of its martensitic transformation and slowly reduces and inverts to a tensile stress state of around 50 MPa for both austenite and martensite.

In Figure 17b, the surface stress evolution for 20MnCr5 and Pyrowear 53 steel grades is shown. Although the overall behavior of the stress evolution is similar for both steel grades, distinct differences are noticeable. Both 20MnCr5 and 18CrNiMo7-6 have the same core transformation temperature of around 400 °C, while Pyrowear 53 steel has a slightly lower core transformation temperature of 392 °C, which is in agreement with Equation (7). After the core transformation, surface stresses rise to ≈250 MPa for the 20MnCr5 sample, a value comparable to that of 18CrNiMo7-6. However, Pyrowear 53 experiences a more pronounced increase in surface stresses, reaching around +320 MPa. Following this sharp increase, the stresses continue to increase gradually up to around 270 MPa and 450 MPa for 20MnCr5 and Pyrowear 53, respectively. The higher maximum tensile stresses of Pyrowear 53 steel are attributed to the high amount of alloying elements, especially silicon and molybdenum, which significantly increase the high-temperature strength, allowing for a more pronounced stress built-up before reaching the yield point of the material.[63–65] Upon reaching the M_s of the surface, around 195 °C for 20MnCr5 and 180 °C for Pyrowear 53, similar to the behavior of 18CrNiMo7-6, tensile stresses are reduced and inverted to compressive stresses for austenite. For martensite, there are also few data points having higher compression stresses in early transformed martensite; however, the following values start from the tensile area, gradually reduce during the cooling and subsequently invert into compressive stresses. In the final state, the 20MnCr5 and Pyrowear 53 grades have very similar residual stresses in austenite, around −200 MPa, while the 18CrNiMo7-6 grade exhibits slightly lower values of around −140 MPa. In martensite, among the three investigated steels, the highest compressive residual stresses at the surface are

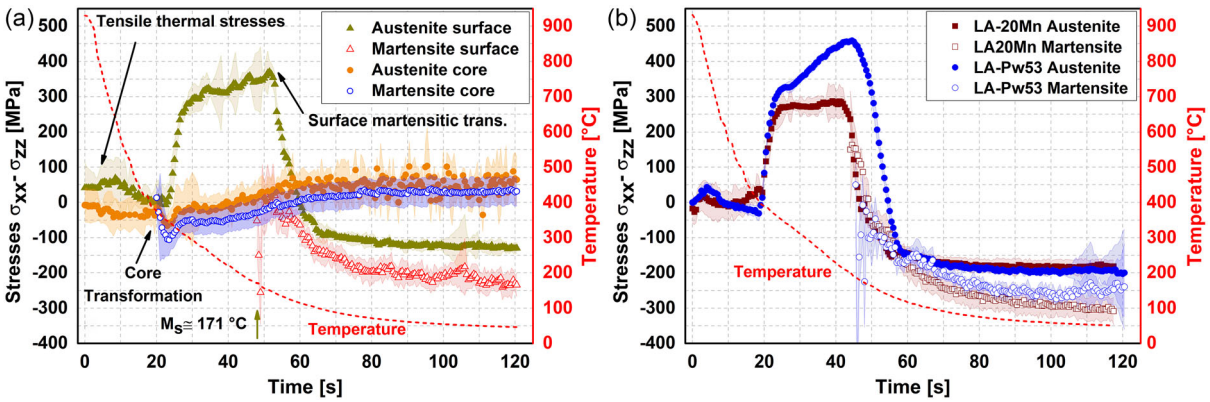

Figure 17. a) Evolution of stresses at the surface and in the core (1 mm below the surface) for sample 18CrNiMo7-6, b) evolution of stresses at the surface for samples 20MnCr5 and Pyrowear 53.

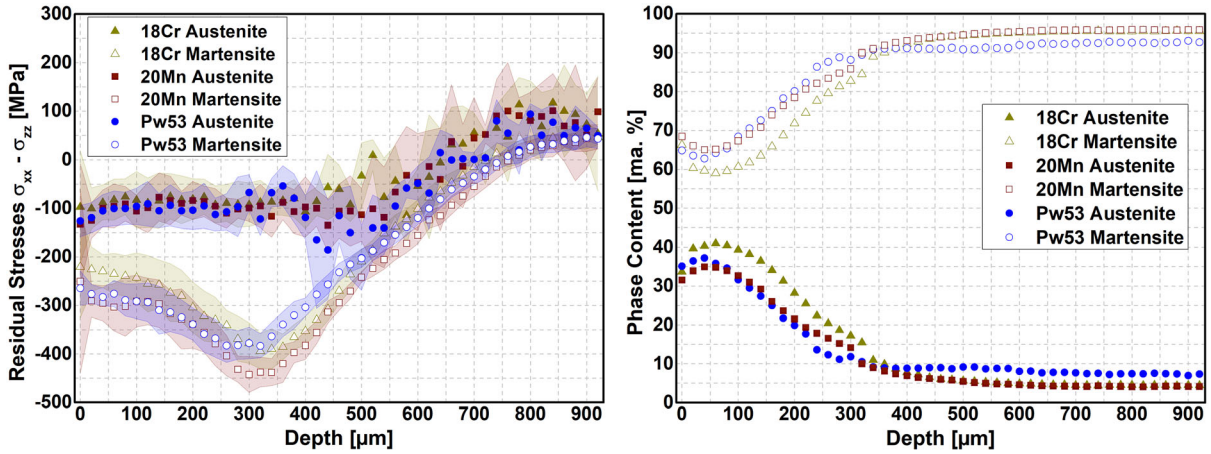

Figure 18. Depth profiles of residual stresses and phase contents of three different steel grades for both austenite and martensite measured at room temperature after the process.

observed for 20MnCr5 with values around −300 MPa, followed by −250 MPa for Pyrowear 53 and −225 MPa for 18CrNiMo7-6.

Figure 18 presents the final residual stress and phase content depth profiles of the three steel grades examined. The residual stress values at the surface are comparable across the grades. For austenite, residual stresses start at −130 MPa for grades 20MnCr5 and Pyrowear 53, and -100 MPa for 18CrNiMo7-6. For all three steel grades, the residual stresses in austenite remain fairly constant until the depth of about 500 µm and gradually shift into tensile stresses in depth between 600 and 700 µm, reaching values of about 100 MPa at a depth of ≈900 µm. The measurements in martensite show that for the steel grades 20MnCr5 and Pyrowear 53, the values at the surface reach ≈−260 MPa, while for the 18CrNiMo7-6 steel slightly, lower values of about −220 MPa were determined. The compressive stresses then increase to a maximum value of about −440 MPa for 20MnCr5, and −375 MPa for 18CrNiMo7-6 and Pyrowear 53 at a comparable depth of about 300 µm.

Since all three steels were carburized under identical process parameters, the observed differences in residual stress evolution arise exclusively from the resulting carbon-gradient shapes and the corresponding amount of martensite formed during quenching. The comparison shows that the amount of formed martensite, rather than the nominal alloy content, is the dominant factor governing the magnitude of compressive stresses. Steels that develop higher martensite fractions at near-surface areas (20MnCr5 and Pyrowear 53) exhibit higher compressive stress regardless of alloying elements, while 18CrNiMo7-6, with a shallower gradient and reduced martensite amount, reaches lower stresses.

3.6. Effect of Carbon Gradient on the Evolution of Stresses

Steel grade 18CrNiMo7-6, carburized with different process parameters to achieve different CGs, was used to study the effect of the CG on the evolution of stresses (see Table 2). During carburizing, after 2 min of boost time, three different diffusion durations were applied to achieve varying carbon depth profiles. After completion of the diffusion step, the samples were quenched while in situ XRD measurements were performed with the gauge volume placed around 10 to 50 µm below the surface.

In **Figure 19**a,b the carbon content depth profile determined from the synchrotron data and the respective retained austenite content over the depth from a synchrotron scan performed after the experiments at room temperature are shown.

The results indicate that the carbon content at the surface of the samples varies from around 1.12 ma% to around 0.62 ma%, while the nominal carbon content of the core is reached at depths between 250 µm and 450 µm.

Figure 20 details the evolution of stresses directly below the surface (10–50 µm below) for 18CrNiMo7-6 samples with varying CGs. The overall stress behavior is consistent with previous observations. At the beginning, all samples show slight tensile stresses in austenite, with a strong increase to about +220 to +300 MPa when the core undergoes martensitic transformation. Since the C-content at the core was not modified, M_s is the same for all samples. Therefore, the temperature at which the sharp increase in stresses starts is almost at the same time for all samples considered here. The level of tensile stresses that are reached increases with the increase in carbon content at the surface/decrease in carburizing depth. In the following time span, tensile stresses slightly increase during cooling and reach, respectively, their maxima shortly before reaching M_s at the surface. At this point, the different surface M_s generate significant differences in the stress evolution during quenching between the three states. The CG-3 sample, having the lowest surface carbon content, undergoes transformation first at a temperature of about 220 °C, followed sequentially by the samples CG-2 and CG-1 as shown with the arrows in Figure 20. Subsequently, tensile residual stresses in austenite gradually reduce for all samples. In the final state, residual stresses in austenite are around −200 MPa for samples CG-2 and CG-3, while the CG-1 sample exhibits a low value close to about −100 MPa. It can also be noticed that tensile stresses in austenite decrease slower after surface martensitic transformation (shown with arrows) for CG-1 compared to the samples CG-2 and CG-3. This is attributed to the very high retained austenite content of sample CG-1, up to about 85 ma%

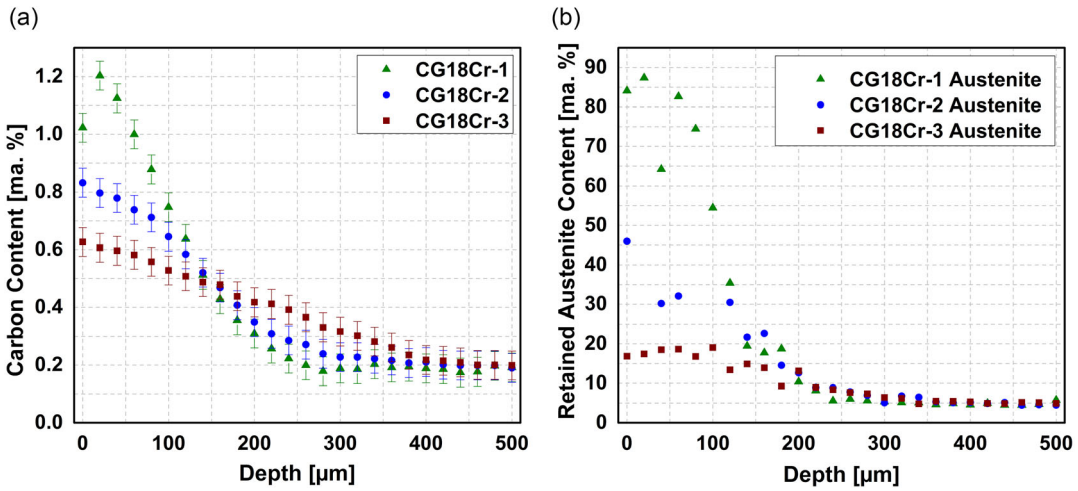

Figure 19. Carbon content a) and retained austenite content b) depth profiles of samples made from steel grade 18CrNiMo7-6 and treated to achieve different CGs (see Table 2).

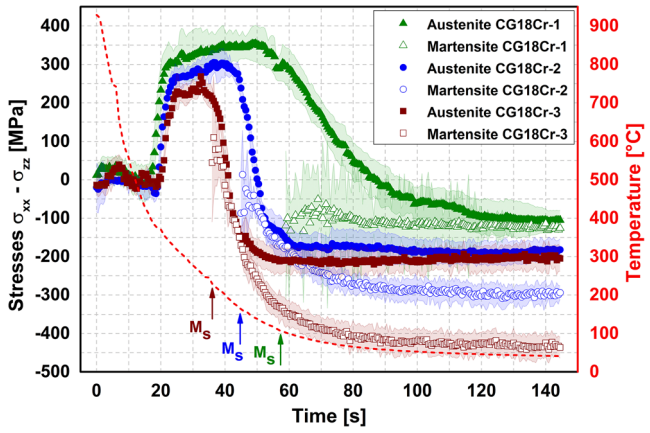

Figure 20. Evolution of stresses at the surface during quenching of 18CrNiMo7-6 samples with varying CGs. The arrows indicate the martensite start temperature (M_s of the corresponding samples using the same colors.

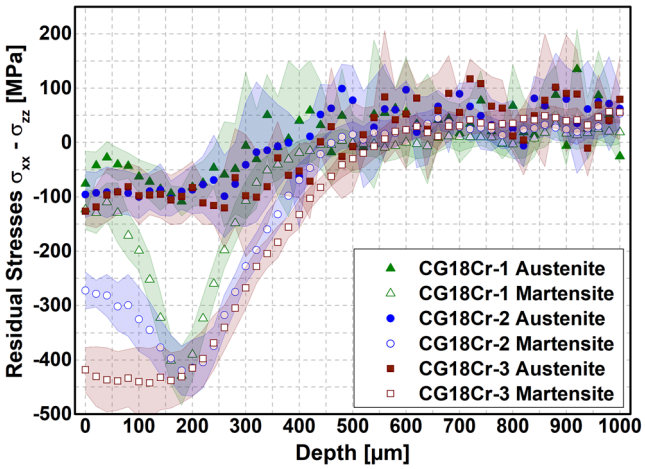

Figure 21. Residual stress depth profiles of 18CrNiMo7-6 samples with varying CGs after quenching to RT.

in the carburized zone, leading to a low amount of martensite formed and therefore, a limited effect of volume increase induced by the transformation occurs.

In the case of the sample CG-3 (lowest surface C-content), the stresses observed in martensite in the early stages of quenching are in tension and continuously shift toward compression up to a value of about −430 MPa, which is by far the highest value in comparison to the other sample states. For sample CG-2, the stresses in martensite start at lower tensile values and reach an intermediate compression state of around −300 MPa at the end of the process. The sample with the highest C-content gradient, CG-1, exhibits an almost constant stress evolution in martensite, of ≈−120 MPa, during the whole transformation until RT.

Figure 21 gives the final residual stress depth profiles of the examined samples measured afterwards at RT. Despite the notable difference of the surface residual stresses in martensite, the maximum compressive residualstress values are very similar for all samples, which is around −420 MPa. For the CG-1 and CG-2 samples, the lower residual stresses at the surface increase sharply and reach maximum values at a depth of around 180 µm, while the CG-3 sample has almost stable residual stress levels up to the same depth. As mentioned earlier, this observation is also highly correlated with the retained austenite depth profile presented in Figure 19, clearly demonstrating that the level of compressive residual stresses in martensite is directly related to the local amount of formed martensite and inversely related to the amount of retained austenite; which is dependent on carbon content. Thus, depths with similar retained austenite amounts exhibit almost similar compressive residual stresses.

This observation is more clearly illustrated in **Figure 22**, which depicts the near-surface stresses of martensite in relation to the amount of austenite during quenching for the three steels under investigation. As martensitic transformation progresses, the residual stress levels generated in martensite are nearly identical across all three sample states. However, due to the higher surface

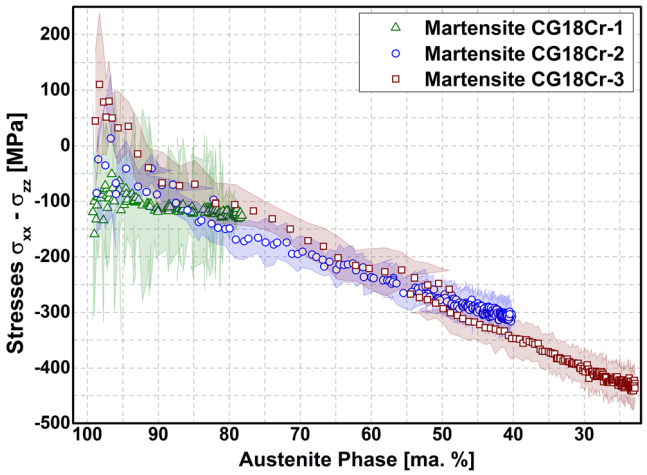

Figure 22. Evolution of residual stresses in martensite at the near-surface region of 18CrNiMo7-6 samples with varying CGs after quenching to RT with respect to the phase fraction of austenite.

carbon content for samples CG-1 and CG-2 compared to sample CG-3, martensitic transformation could not advance until higher residual stress levels were reached. However, as shown in Figure 21, areas exhibiting a similar degree of martensitic transformation also display comparable magnitudes of residual stresses in martensite in a depth of about 200 µm.

4. Conclusions

In the present study, complete LPC treatments were conducted in a specially designed experimental heat treatment chamber with four different steel grades—namely 14NiCrMo13-4, 20MnCr5, 18CrNiMo7-6, and Pyrowear 53—while material analysis was carried out by means of in situ HEXRD. Based on the results presented, the following main conclusions can be drawn: 1) During the boost steps, the austenite solubility limit was reached in a few seconds due to the rapid carbon uptake rate from the atmosphere inside the chamber into the sample, regardless of the investigated parameters. Subsequently, the carbon content decreased for all samples due to diffusion of carbon, despite the continued presence of acetylene in the chamber atmosphere. This phenomenon is seen as strong evidence for the deceleration of carbon uptake due to surface carbon accumulation and carbide layer formation at the surface of the material. This phenomenon was especially prevalent for steel grade Pyrowear 53, which has more carbide-forming elements compared to the other investigated grades. Since complete elimination of carbide formation is challenging due to its early onset, it is recommended to shorten the durations of the individual boost steps and increase the total number of boost steps. This approach maintains the same total carbon supply while allowing sufficient time for the carbides to dissolve, and it also reduces the formation of stable Mo-carbides. 2) Carbides formed at the surface of the material during the first seconds of the boost steps started to dissolve during the subsequent diffusion steps. The formation and dissolution kinetics of the carbides are highly dependent on the steel grade and carbide type. The most dominant carbides formed during the boost step were in the form of M_3C; however, the results indicate varying contributions from more stable alloy carbides in the form of M_6C, depending on the specific steel grade. 3) After a 25 min diffusion step following a 2 min boost step at 930 °C, carbides still remained present in the Pyrowear 53 steel grade. This persistence is attributed to the higher molybdenum content, which leads to the formation of more stable carbides such as M_2C and M_3C_2 as well as the stabilization of M_3C carbides. Additionally, it was observed that the carbide content increased with the number of boost steps, indicating that the repeated carbon enrichment further promotes carbide formation. 4) During quenching, early-formed martensite, especially martensite that was formed in the first 5 s, exhibited a significantly lower c/a ratio compared to martensite formed later. This is attributed to the early phase transformation of austenite grains having lower carbon content. On the other hand, instantaneous self-tempering, evolution of second-order stresses between austenite and martensite, and carbon redistribution/ordering are also possible factors leading to the lower tetragonality of martensite. 5) Regarding the investigation of the effect of the amount of acetylene, two experiments were conducted with different durations of the boost steps. Although carbon contents were similar during the initial boost step and early minutes of the first diffusion step, the accumulated carbon at the surface and possibly formed carbides contributed more to the overall carbon content for the sample carburized with a higher boost duration. This effect becomes more pronounced with each further boost/diffusion cycle. 6) The evolution of phase-specific stresses during quenching was systematically analyzed and could be tracked experimentally in both dominant phases, that is, in austenite and martensite, in the surface region and below the carburized region. Thermal stresses were generated at the surface in the tensile direction during the initial stages of the quenching step due to thermal gradients of the sample. Subsequently, a martensitic transformation of the core was clearly identified, which creates an expansion at the core. This expansion caused a sharp increase of tensile stresses at the surface. As the transformation progresses, the near-surface and the very surface regions undergo martensitic transformation, inducing a volume increase. However, this expansion is constrained by the already hardened, rigid core, resulting in a gradual mitigation and reversal of tensile stresses to compressive stresses at the surface. Differences in the transformation temperatures along the CG for the samples with different carbon depth profiles highly affect the maximum stresses reached in both austenite and martensite phases. In summary, the locally formed martensite determines the residual stresses in the martensite regardless of the depth.

Future work should focus on extending the in situ methodology to more complex component geometries, where nonuniform heat transfer or geometry-dependent stress fields are present, and include process simulation. Such studies would help bridge the gap between the current study and the industrial LPC component.

Acknowledgements

The authors gratefully acknowledge the support from the German Research Foundation (DFG) for funding this research under the collaborative project EP-128/2-2 | GI-376/15-2 (DFG project no. 399551201) and

Deutsches Elektronen-Synchrotron (DESY) for granting beam time. Furthermore, the authors would like to thank Alexander Kohl from IWT and Marcel Miatke from KIT for their participation in the measuring campaign at DESY and their engagement in the planning and realization of the process chamber components.

Open Access funding enabled and organized by Projekt DEAL.

Conflict of Interest

The authors declare no conflict of interest.

Author Contributions

Ogün Baris Tapar: conceptualization: (equal); data curation: (equal); formal analysis: (equal); investigation: (equal); methodology: (equal); resources: (equal); software: (equal); validation: (equal); visualization: (equal); writing—original draft: (equal). **Michael Georg Zürn**: conceptualization: (supporting); data curation: (supporting); formal analysis: (supporting); investigation: (supporting); methodology: (supporting); software: (supporting); validation: (supporting); visualization: (supporting); writing—original draft: (supporting); writing—review & editing: (supporting). **Jens Gibmeier**: conceptualization: (lead); data curation: (lead); formal analysis: (lead); funding acquisition: (lead); investigation: (lead); methodology: (lead); project administration: (lead); resources: (lead); software: (lead); supervision: (lead); validation: (lead); visualization: (lead); writing—original draft: (lead); writing—review & editing: (lead). **Antonio Carlos de Figueiredo Silveira**: conceptualization: (supporting); data curation: (supporting); formal analysis: (supporting); investigation: (supporting); methodology: (supporting); software: (supporting); visualization: (supporting); writing original draft: (supporting). **Matthias Steinbacher**: conceptualization: (supporting); investigation: (supporting); methodology: (supporting); software: (supporting); supervision: (supporting); validation: (supporting). **Norbert Schell:** data curation: (supporting); formal analysis: (supporting); investigation: (supporting); software: (supporting); supervision: (supporting). **Jérémy Epp**: conceptualization: (lead); data curation: (lead); formal analysis: (lead); funding acquisition: (lead); investigation: (lead); methodology: (lead); project administration: (lead); resources: (lead); software: (lead); supervision: (lead); validation: (lead); visualization: (lead); writing—original draft: (lead); writing—review & editing: (lead).

Data Availability Statement

Research data are not shared.

Keywords

carbides, carbon diffusion, case-hardening, in situ synchrotron diffraction, low-pressure carburizing, residual stress, Rietveld refinement

Received: October 1, 2025
Revised: November 28, 2025
Published online:

[1] B. Edenhofer, D. Joritz, M. Rink, *Thermochem. Surf. Eng. Steels Improv. Mater. Perform.*, Woodhead Publishing. **2015**, pp. 485–553, https://doi.org/10.1533/9780857096524.3.485.
[2] J. Rudnizki, B. Zeislmair, U. Prahl, W. Bleck, *Steel Res. Int.* **2010**, *81*, 472.
[3] T. Bensabath, M. D. Le, H. Monnier, P. A. Glaude, *Chem. Eng. Sci.* **2019**, *202*, 84.
[4] V. G. Knorre, D. Tanke, T. Thienel, H. G. Wagner, *Symp. Combust.* **1996**, *26*, 2303.
[5] K. Yada, O. Watanabe, *Comput. Fluids* **2013**, *79*, 65.
[6] O. A. Rokstad, O. A. Lindvaag, A. Holmen, *Int. J. Chem. Kinet.* **2014**, *46*, 104.
[7] H. Westeren, E. Gronquist, D. Taft, V. Scotto, Method of vacuum carburizing, US3796615A **1974**.
[8] R. Gorockiewicz, *Vacuum* **2011**, *86*, 448.
[9] R. Gorockiewicz, A. Łapiński, *Vacuum* **2010**, *85*, 429.
[10] G. H. Kwon, H. Park, Y. K. Lee, K. Moon, *Metals* **2024**, *14*, 29.
[11] E. Wołowiec-Korecka, M. Korecki, L. Klimek, *Coatings* **2022**, *12*, 337.
[12] K. Tanaka, H. Ikehata, H. Takamiya, H. Mizuno, *ISIJ Int.* **2012**, *52*, 134.
[13] M. Zajusz, K. Tkacz-Śmiech, M. Danielewski, *Surf. Coatings Technol.* **2014**, *258*, 646.
[14] X. An, Y. Tian, B. Wang, T. Jia, H. Wang, Z. Wang, *Surf. Coatings Technol.* **2021**, *421*, 127348.
[15] H. Wang, B. Wang, Z. Wang, Y. Tian, R. D. K. Misra, *J. Mater. Sci. Technol.* **2019**, *35*, 1218.
[16] L. Yin, X. Ma, G. Tang, Z. Fu, S. Yang, T. Wang, L. Wang, L. Li, *Surf. Coatings Technol.* **2019**, *358*, 654.
[17] Y. He, X. J. Zeng, L. Q. Li, N. Li, J. B. Niu, X. X. Ma, *Surf. Coatings Technol.* **2024**, *484*, 130868.
[18] V. A. Esin, B. Denand, Q. Le Bihan, M. Dehmas, J. Teixeira, G. Geandier, S. Denis, T. Sourmail, E. Aeby-Gautier, *Acta Mater.* **2014**, *80*, 118.
[19] M. Villa, K. Pantleon, M. A. J. Somers, *J. Alloys Compd.* **2013**, *557*, 543.
[20] E. J. Pickering, J. Collins, A. Stark, L. D. Connor, A. A. Kiely, H. J. Stone, *Mater. Charact.* **2020**, *165*, 110355.
[21] G. G. Ribamar, J. D. Escobar, A. Kwiatkowski da Silva, N. Schell, J. A. Ávila, A. S. Nishikawa, J. P. Oliveira, H. Goldenstein, *Acta Mater.* **2023**, *247*, 118742.
[22] B. Denand, V. A. Esin, M. Dehmas, G. Geandier, S. Denis, T. Sourmail, E. Aeby-Gautier, *Materialia* **2020**, *10*, 100644.
[23] S. Wang, A. A. Kistanov, G. King, S. Ghosh, H. Singh, S. Pallaspuro, A. Rahemtulla, M. Somani, J. Kömi, W. Cao, M. Huttula, *Acta Mater.* **2021**, *221*, 117361.
[24] S. Y. P. Allain, S. Gaudez, G. Geandier, F. Danoix, M. Soler, M. Goune, *Scr. Mater.* **2020**, *181*, 108.
[25] S. C. Bodner, M. Meindlhumer, T. Ziegelwanger, H. Winklmayr, T. Hatzenbichler, C. Schindelbacher, B. Sartory, M. Krobath, W. Ecker, N. Schell, J. Keckes, *J. Mater. Res. Technol.* **2021**, *11*, 1396.
[26] J. Teixeira, K. Jeyabalan, G. Geandier, J. Dulcy, B. Denand, M.-R. Chini, S. D. Catteau, M. Courteaux, S. Denis, *Acta Mater.* **2024**, *275*, 120065.
[27] O. B. Tapar, J. Epp, M. Steinbacher, J. Gibmeier, *Metall. Mater. Trans. A Phys. Metall. Mater. Sci.* **2021**, *52*, 1.
[28] J. C. Oxley, J. L. Smith, F. L. Steinkamp, J. Gorawara, V. Kanazirev, *J. Chem. Heal. Saf.* **2017**, *24*, 26.
[29] N. Schell, A. King, F. Beckmann, T. Fischer, M. Müller, A. Schreyer, *Mater. Sci. Forum*, Trans Tech Publications Ltd **2014**, pp. 57–61, https://doi.org/10.4028/www.scientific.net/MSF.772.57.
[30] G. Ashiotis, A. Deschildre, Z. Nawaz, J. P. Wright, D. Karkoulis, F. E. Picca, J. Kieffer, *J. Appl. Crystallogr.* **2015**, *48*, 510.
[31] A. P. Hammersley, S. O. Svensson, M. Hanfland, A. N. Fitch, D. Häusermann, *High Press. Res.* **1996**, *14*, 235.
[32] A. A. Coelho, *An, J. Appl. Crystallogr.* **2018**, *51*, 210.
[33] R. W. Cheary, A. Coelho, *J. Appl. Crystallogr.* **1992**, *25*, 109.
[34] R. E. Dinnebier, A. Leineweber, J. S. O. Evans, Rietveld refinement: Practical powder diffraction pattern analysis using TOPAS, De Gruyter STEM **2018**. https://doi.org/10.1515/9783110461381.
[35] F. Heidelbach, C. Riekel, H. R. Wenk, *J. Appl. Crystallogr.* **1999**, *32*, 841.
[36] S. J.B. Kurz, S. R. Meka, N. Schell, W. Ecker, J. Keckes, E. J. Mittemeijer, *Acta Mater.* **2015**, *87*, 100.
[37] U. Welzel, J. Ligot, P. Lamparter, A. C. Vermeulen, E. J. Mittemeijer, *J. Appl. Crystallogr.* **2005**, *38*, 1.

[38] F. Richter, *Die Physikalischen Eigenschaften Der Stähle -Das 100 -Stähle -Programm -Teil I: Tafeln Und Bilder*, Mühlheim an der Ruhr **2010**.
[39] B. B. He, *Two-Dimensional X-Ray Diffraction*, 2nd ed., John Wiley & Sons, Inc., Hoboken **2018**, https://doi.org/10.1002/9781119356080.
[40] O. B. Tapar, M. Steinbacher, J. Gibmeier, J. Epp, *Adv. Eng. Mater.* **2021**, *23*, 2100124.
[41] O. B. Tapar, M. Steinbacher, J. Gibmeier, N. Schell, J. Epp, *HTM - J. Heat Treat. Mater.* **2021**, *76*.
[42] M. Onink, C. M. Brakman, F. D. Tichelaar, E. J. Mittemeijer, S. van der Zwaag, J. H. Root, N. B. Konyer, *Scr. Metall. Mater.* **1993**, *29*, 1011.
[43] S. M. C. Van Bohemen, *Mater. Sci. Technol.* **2012**, *28*, 487.
[44] L. Cheng, A. Böttger, T. H. de Keijser, E. J. Mittemeijer, *Scr. Metall. Mater.* **1990**, *24*, 509.
[45] M. Villa, F. Niessen, M. A. J. Somers, *Metall. Mater. Trans. A Phys. Metall. Mater. Sci.* **2018**, *49*, 28.
[46] P. Huyghe, M. Caruso, J. L. Collet, S. Dépinoy, S. Godet, *Mater. Sci. Eng. A* **2019**, *743*, 175.
[47] H. K. D. H. Bhadeshia, *Met. Sci.* **1983**, *17*, 151.
[48] D. H. Sherman, S. M. Cross, S. Kim, F. Grandjean, G. J. Long, M. K. Miller, *Metall. Mater. Trans. A Phys. Metall. Mater. Sci.* **2007**, *38*, 1698.
[49] C. Lerchbacher, S. Zinner, H. Leitner, *Micron* **2012**, *43*, 818.
[50] K. A. Taylor, M. Cohen, *Prog. Mater. Sci.* **1992**, *36*, 151.
[51] Yu. M. Lakhtin, V. D. Kal'ner, V. K. Sedunov, A. Smirnova, Effect of preliminary cold deformation on carburizing of steel, Chemicothermal Treatment Pages **1971**, pp. 1016–1020
[52] O. K. Rowan, R. D. Sisson, *J. Phase Equilibria Diffus.* **2009**, *30*, 235.
[53] G. Parrish, *Carburizing : Microstructures and Properties*, ASM International, Ohio **1999**, https://doi.org/10.31399/asm.tb.cmp.9781627083379.
[54] R. P. Agarwala, M. C. Naik, M. S. Anand, A. R. Paul, *J. Nucl. Mater.* **1970**, *36*, 41.
[55] M. Romedenne, F. Rouillard, D. Hamon, B. Malard, D. Monceau, *Corros. Sci.* **2019**, *159*, 108147.
[56] R. U. Khan, D. Buchholz, F. Graf, R. Reimert, *Int. J. Chem. React. Eng.* **2009**, *7*, A10.
[57] H. K. D. H. Bhadeshia, *Prog. Mater. Sci.* **2012**, *57*, 268.
[58] A. Bénéteau, P. Weisbecker, G. Geandier, E. Aeby-Gautier, B. Appolaire, *Mater. Sci. Eng. A.* **2005**, *393*, 63.
[59] J. E. Bridge, G. N. Maniar, T. V. Philip, *Metall. Mater. Trans. B* **1971**, *2*, 2209.
[60] M. Umemoto, Z. G. Liu, K. Masuyama, K. Tsuchiya, *Scr. Mater.* **2001**, *45*, 391.
[61] M. R. Ghomashchi, *Acta Mater.* **1998**, *46*, 5207.
[62] W. Liu, Y. Guo, Y. Cao, J. Wang, Z. Hou, M. Sun, B. Xu, D. Li, *J. Alloys Compd.* **2022**, *889*, 161755.
[63] H. K. D. H. Bhadeshia, R. W. K. Honeycombe, *Steels: Microstructure and Properties*, 4th ed., Elsevier Inc, Amsterdam **2017**.
[64] S. Jung, C. Jeon, Y. H. Jo, W. M. Choi, B. J. Lee, Y. J. Oh, S. Jang, S. Lee, *Mater. Sci. Eng. A* **2016**, *656*, 190.
[65] P. J. Grobner, W. C. Hagel, *Metall. Trans. A* **1980**, *11*, 633.